



# Numerical instabilities of spherical shallow water models considering small equivalent depths

Pedro S. Peixoto <sup>a\*</sup> and John Thuburn <sup>b</sup> and Michael J. Bell <sup>c</sup>

<sup>a</sup> Instituto de Matemática e Estatística, Universidade de São Paulo, Brazil

<sup>b</sup> College of Engineering, Mathematics and Physical Sciences, University of Exeter, UK

<sup>c</sup> Met Office, Fitzroy Rd, Exeter, UK

\*Correspondence to: pedrosp@ime.usp.br

Shallow water models are often adopted as an intermediate step in the development of atmosphere and ocean models, though they are usually tested only with fluid depths relevant to barotropic fluids. Here we investigate numerical instabilities emerging in shallow water models considering small fluid depths, which are relevant for baroclinic fluids. Different numerical instabilities of similar nature are investigated. The first one is due to the adoption of the vector invariant form of the momentum equations, related to what is known as the Hollingsworth instability. We provide examples of this instability with finite volume and finite element schemes used in modern quasi-uniform spherical grid based models. The second is related to an energy conserving form of discretization of the Coriolis term in finite difference schemes on latitude-longitude global models. Simple test cases with shallow fluid depths are proposed as a means of capturing and predicting stability issues that can appear in three-dimensional models using only two-dimensional shallow-water codes.

*Key Words:* Hollingsworth instability, shallow water equations, vector invariant momentum equations, equivalent depth

*Received ...*

13 **1. Introduction**

14 In the development of an ocean or atmosphere model it is important to establish that the numerical methods used are stable. In practice,  
 15 a mathematical stability analysis might not be tractable, for example if the geometry, grid structure, or background state are not simple  
 16 enough; in that case stability can only be determined by empirical tests. It may also be the case that a mathematical analysis is not done  
 17 because a particular type of instability was not anticipated. It is highly desirable to be able to identify any instability of some candidate  
 18 numerical method before investing the effort to develop a three-dimensional model. Shallow water models are often adopted as an  
 19 intermediate step in the development of atmosphere and ocean models and can be useful in testing the stability of numerical methods.  
 20 However, standard numerical test cases (e.g. [Williamson \*et al.\* 1992](#); [Galewsky \*et al.\* 2004](#); [Shamir and Paldor 2016](#)) are usually run  
 21 with fluid depths of thousands of metres, relevant to barotropic fluids. In this paper we point out the usefulness of spherical shallow  
 22 water models run with very shallow fluid depths, mimicking the internal modes of three-dimensional models, for testing the stability  
 23 of numerical methods.

24 [Hollingsworth \*et al.\* \(1983\)](#) discovered that an implementation of a well known energy and enstrophy conserving scheme, originally  
 25 due to Sadourny, when used in a hydrostatic primitive equation model ([Burridge and Haseler 1977](#)), was prone to near-grid-scale  
 26 instabilities, with severe consequences for high resolution forecasts. This kind of instability is intrinsically related to the use of the  
 27 vector invariant form of the momentum equations (e.g. [Vallis 2006](#)), which expresses the advection of momentum as

$$\mathbf{v} \cdot \nabla \mathbf{v} = \nabla K + \zeta \mathbf{k} \times \mathbf{v}, \quad (1)$$

28 where  $\mathbf{v} = (u, v)$  defines the horizontal velocities,  $K = \|\mathbf{v}\|^2/2$  is the kinetic energy,  $\zeta = \mathbf{k} \cdot \nabla \times \mathbf{v}$  is the relative vorticity and  $\mathbf{k}$  is  
 29 a unit vector pointing normal to the horizontal surface. Expanding the differential expressions, and looking at the equations for each  
 30 velocity component separately, one notices that on the left hand side of the above relations there are no derivatives of  $v$  in the  $u$  equation,  
 31 and no derivatives of  $u$  in the  $v$  equation. In contrast, we see that these derivatives exist in each of the two terms on the right hand sides,  
 32 respectively, but they cancel out. The cancellation is a general feature of this formulation of the equation, and exists independently of  
 33 the particular choice of coordinate system.

34 In numerical schemes, this cancellation is not always exact, and this may lead to stability issues. This is what happens with the  
 35 original energy and enstrophy conserving scheme of Sadourny ([Burridge and Haseler 1977](#)), hereafter referred to as the ‘een’ scheme.  
 36 [Hollingsworth \*et al.\* \(1983\)](#) proposed a modification of the scheme to ensure cancellation at a discrete level of the linearized equations,  
 37 avoiding the instability while preserving its conservation properties. Similarly, the energy and enstrophy conserving scheme of [Arakawa  
 38 and Lamb \(1981\)](#), hereafter referred to as ‘AL’ scheme, was also shown to be prone to such instabilities, and again a modification was  
 39 proposed to avoid it.

40 There has been a renewed interest in these instabilities, as the vector-invariant form of the momentum equations have recently  
 41 been adopted in many novel atmospheric and ocean models on quasi-uniform spherical grids (e.g. [Tomita \*et al.\* 2008](#); [Wan \*et al.\*  
 42 2013](#); [Ringler \*et al.\* 2013](#); [Skamarock \*et al.\* 2012](#); [Gassmann 2013](#)). As a consequence, novel high resolution ocean and atmosphere  
 43 models are presenting instabilities of a similar nature (e.g. [Skamarock \*et al.\* 2012](#); [Gassmann 2013](#)). A problematic point is that such  
 44 instabilities are only being detected once the full 3D model is implemented, as no trace of instability is usually detected in shallow  
 45 water prototypes.

46 [Bell \*et al.\* \(2017\)](#), hereafter referred to as BPT, examined the instability for the two well known energy and enstrophy conserving  
 47 schemes, the ‘een’ and ‘AL’ schemes, for the vector invariant hydrostatic Boussinesq equations. As found by [Hollingsworth \*et al.\*  
 48 \(1983\)](#), the schemes were shown to be linearly unstable for height coordinate models. Also, BPT showed that it is possible to detect  
 49 such instabilities on shallow water versions of the schemes, as long as the model adopts a small equivalent depth, that is, the shallow  
 50 water layer is very thin. This allows easy testing of novel and existing schemes for unstable linear modes of similar nature to the  
 51 original instability detected by [Hollingsworth \*et al.\* \(1983\)](#). All the analysis of BPT was performed for planar quadrilateral grids, but it  
 52 suggests a way of testing for the instability on more general discrete domains, such as the quasi-uniform spherical ones.

53 Shallow water models considering small equivalent depths are directly related to reduced gravity layer models (e.g. [Vallis 2006](#)).  
 54 Reducing the inertia-gravity wave speed increases the importance of the nonlinear terms, such as advection terms in the shallow water  
 55 equations, and so exacerbates the effect of any numerical errors in those terms. [Gassmann \(2011\)](#) shows an experiment that mimics  
 56 the case of relatively small equivalent depths occurring in atmospheric models using a planar triangular-hexagonal grid shallow water  
 57 model. The results allow interpretation, within a simpler 2D shallow water framework, of how a checker-board divergence mode is  
 58 expected to interfere in a 3D model. Similarly, [Peixoto \(2016\)](#) uses a shallow water experiment with reduced depth to illustrate and  
 59 foresee inaccuracies that might appear due to the finite volume discretizations of the nonlinear terms on quasi-uniform spherical grids.

60 The main goal of this paper is to discuss possible numerical instabilities that may arise in shallow water spherical models when  
 61 small equivalent depths are adopted. Two different kinds of instabilities that appear in linear analysis for the equations linearized about  
 62 a non-resting basic state with small depth are analysed. One of the instabilities is the one arising from the use of the vector invariant  
 63 form of the momentum equations, which is of similar nature to that of [Hollingsworth \*et al.\* \(1983\)](#) and is what motivated this study.  
 64 The other instability occurs in a latitude-longitude C-staggered semi-Lagrangian semi-implicit finite differences model, as used, for  
 65 example, in the Unified Model of the UK MetOffice, also known as ENDGame ([Wood \*et al.\* 2014](#)). The scheme used in ENDGame is  
 66 based on the discretization proposed in [Zerroukat \*et al.\* \(2009\)](#), where the Coriolis term discretization, brought forward from [Thuburn  
 67 and Staniforth \(2004\)](#), was inspired by the work of [Arakawa and Lamb \(1981\)](#). Therefore, the two cases analysed are more intimately  
 68 related than it would seem at first, as will be discussed in what follows.

69 A key concept used in this paper is that the stability analysis of three-dimensional models may be done by separating the linear  
 70 modes into horizontal and vertical parts, and these are connected by equivalent depths. A discussion of the equivalent depths emerging in  
 71 typical three-dimensional sets of equations is presented in Section 2; followed by a discussion of how different vertical coordinates may  
 72 be interpreted either using depth-weighted or non-depth-weighted vorticity terms in shallow water systems. Based on these discussions,  
 73 we can thereafter limit our attention only to shallow water equations, but with conclusions that can be interpreted for three-dimensional  
 74 models.

75 In Section 3 we discuss the influence of the Coriolis force in the Hollingsworth instability, showing that the instability exists even  
 76 in models without Coriolis terms. Section 4 presents the common framework of tests and methods that will be used to investigate  
 77 several different spherical shallow water models. Section 5 examines the Hollingsworth instability in quasi-uniform spherical grids,  
 78 such as cubed and icosahedral spheres, for finite volume and finite element schemes. Section 6 analyses the instabilities detected for  
 79 ENDGame, starting from an analytical examination of the linear modes on a plane, followed by numerical experiments on the sphere.

## 80 2. From 3D models to 2D analyses

### 81 2.1. Equivalent depths in 3D models

82 A relatively good approximation to ocean dynamics is to consider the hydrostatic, incompressible, adiabatic, Boussinesq equations. The  
 83 linearized Boussinesq equations enjoy separable solutions (Gill 1982; Vallis 2006), and the important terms connecting the vertical and  
 84 horizontal modes are the equivalent depths, which are eigenvalues of the vertical mode problem. These are named equivalent depths  
 85 because they give rise to shallow water systems with such mean fluid depth. Bell *et al.* (2017) analyse the Boussinesq equations  
 86 considering a constant Coriolis parameter plane and two vertical coordinate systems: height and isopycnal. The numerical vertical  
 87 modes are investigated for a Lorenz and a Charney-Phillips staggering, respectively for height and isopycnal coordinates, and estimates  
 88 of equivalent depths for real application parameters are discussed. On a Charney-Phillips grid, considering 100 vertical layers, typical  
 89 ocean parameters can result in equivalent depths of less than a metre. The Lorenz grid has equivalent depths inversely proportional to  
 90 the square of the number of modes, so when many vertical levels (e.g. 100) are used, this may result in equivalent depths smaller than  
 91 millimetres.

92 Many weather and climate models adopt the primitive equations for modelling the atmospheric dynamics (Lauritzen *et al.* 2011;  
 93 Holton and Hakim 2012). Similar vertical versus horizontal separation is also possible for the linearized primitive equations, and  
 94 again the key connecting parameters are the equivalent depths (Tribbia and Temam 2011). Terasaki and Tanaka (2007) investigated the  
 95 equivalent depths occurring in the primitive equations. For a fully spectral analysis and standard atmospheric parameters, considering  
 96 22 vertical spectral modes, the minimum equivalent depth calculated was about 8m. Also, Kasahara and Puri (1981) perform a full  
 97 analysis of the 3D modes and calculate the equivalent depths emerging for this kind of equation set for a sigma coordinate model. An  
 98 example for a model discretized vertically with finite differences with 9 sigma levels shows that the smallest equivalent depth is 3m.  
 99 The smaller equivalent depth estimated in Kasahara and Puri (1981), even with only 9 levels, is due to use of a vertical finite differences  
 100 scheme, whereas Terasaki and Tanaka (2007) consider a spectral vertical analysis.

101 High resolution global atmospheric models often adopt the full, non-hydrostatic, compressible Euler equations. Under the shallow  
 102 atmosphere approximation, the linear compressible Euler equations have normal mode solutions that separate into a product of a vertical  
 103 structure function and a horizontal structure function; however, in contrast to the hydrostatic case, the vertical structure equation  
 104 involves the mode frequency (Daley 1988). Consequently, the horizontal structure equation no longer has a single equivalent depth  
 105 independent of the mode frequency. Nevertheless, for gravity modes with large vertical wavenumber, which are the most problematic  
 106 modes for the instabilities of interest here, non-hydrostatic effects are rather weak. Therefore, analysis based on the hydrostatic  
 107 assumption, particularly the smallest equivalent depths, should give a useful indication of model behaviour in the non-hydrostatic  
 108 case too.

109 To summarise, in realistic atmosphere and ocean models the equivalent depth of higher internal modes is expected to be small, only  
 110 a few metres or smaller, and can be much smaller depending on the vertical coordinate and grid adopted.

### 111 2.2. Form of the vorticity term, and relation to vertical coordinate systems

112 For the vector invariant form of the shallow water equations there are two distinct ways of writing the vorticity term:

$$(f + \zeta)\mathbf{k} \times \mathbf{v} \quad \text{and} \quad q\mathbf{k} \times \eta\mathbf{v}, \quad (2)$$

113 where  $f$  is the Coriolis parameter,  $\eta$  is the fluid depth, and  $q = (f + \zeta)/\eta$  is the potential vorticity. We will refer to these as the non-  
 114 depth-weighted form and depth-weighted form, respectively. For the continuous equations the two forms are equivalent, but this is no  
 115 longer the case after discretization. The depth-weighted form is attractive because it facilitates the design of numerical schemes that  
 116 conserve potential-vorticity-related quantities such as potential enstrophy (Arakawa and Lamb 1981; Ringler *et al.* 2010). Importantly,  
 117 the presence or absence of depth weighting can affect the stability of the scheme (BPT, also see below).

118 A similar distinction arises when the advective form of the momentum equation is used, except that now only the Coriolis term is  
 119 affected. The non-depth-weighted and depth-weighted forms are

$$f\mathbf{k} \times \mathbf{v} \quad \text{and} \quad \frac{f}{\eta}\mathbf{k} \times \eta\mathbf{v}, \quad (3)$$

120 respectively.

121 When analysing the stability of a three-dimensional numerical method by separation into a vertical structure problem and a shallow  
 122 water problem, it is important to determine which form of the vorticity term is appropriate. The form of the vorticity term in a three  
 123 dimensional model is closely related to the type of vertical coordinate it uses.

124 Layer-based vertical coordinates offer the flexibility to choose either a depth-weighted or a non-depth-weighted discretization of the  
 125 vorticity term, and the depth-weighted option is a common choice. By ‘layer-based vertical coordinate’ we mean one that carries some  
 126 quasi-Lagrangian information about the thickness of material layers. Common examples of layer-based coordinates include isentropic,  
 127 isopycnal, and Lagrangian coordinates. Throughout much of the atmosphere diabatic heating is weak and potential temperature  $\theta$  is  
 128 approximately materially conserved. Thus isentropic surfaces (surfaces of constant  $\theta$ ) are approximately Lagrangian surfaces, and a  
 129 coordinate system with  $\theta$  as the vertical coordinate provides a quasi-Lagrangian coordinate system that has some attractive features for

130 atmospheric modelling (e.g. [Hsu and Arakawa 1990](#)). In an analogous way, potential density is approximately materially conserved  
 131 throughout much of the ocean, providing the basis for an isopycnal vertical coordinate (e.g. [Bleck and Boudra 1981](#)). For atmospheric  
 132 modelling a Lagrangian vertical coordinate, in which a set of material surfaces are used to define the vertical coordinate, has also been  
 133 used (e.g. [Lin 2004](#)). In practice all such models require some measures to ensure that model layers do not fold over or become too thin.  
 134 Nevertheless, they all carry information about the thickness of quasi-Lagrangian layers and so can use the depth-weighted vorticity or  
 135 Coriolis terms.

136 In level-based coordinates, on the other hand, the non-depth-weighted form of the vorticity term is generally used. Level-based  
 137 models adopt a monotonic variable, such as geometric height, to define fixed vertical levels. For the present discussion, pressure-based  
 138 coordinates and mass-based coordinates, including their terrain-following variants, should also be thought of as level-based. Although  
 139 the height of pressure levels or mass levels can vary in time, these variations are relatively small. Level-based coordinate systems do  
 140 not carry direct information on the thickness of material layers. In principle some estimate of material layer depth such as  $(\partial\theta/\partial z)^{-1}$   
 141 could be calculated in order to use a depth-weighted vorticity term; however, the numerical errors in this estimate would affect small  
 142 vertical scales and would need to be accounted for in any stability analysis.

143 In some height-, pressure-, or mass-based atmospheric models the vorticity or Coriolis terms are weighted by density or by a pseudo-  
 144 density proportional to density times model layer thickness (e.g. [Skamarock et al. 2012](#); [Wood et al. 2014](#); [Dubos et al. 2015](#)). However,  
 145 local variations in density are relatively small, so this density-weighting does not have the same effect as depth-weighting. Similarly,  
 146 the thickness of model layers does not correspond to the thickness of material layers ([Arakawa 2000](#)), so pseudo-density-weighting  
 147 does not have the same effect as depth-weighting. Therefore, models based on such coordinate systems must be interpreted as using  
 148 non-depth-weighted vorticity or Coriolis terms and analysed accordingly.

### 149 3. The role of the Coriolis force in the Hollingsworth instability

150 We discussed in the introduction how the Hollingsworth instability is connected to the vector invariant form of the momentum equations  
 151 through the lack of a certain discrete cancellation. The term responsible for the lack of cancellation solely involves momentum  
 152 advection, so it might be expected that the Coriolis term should play no role in the existence of such instability.

153 [Lazić et al. \(1986\)](#) observed that real data runs of a 3D finite-difference ECMWF\* model, which used the original energy- and  
 154 enstrophy-conserving ‘een’ scheme, collapsed after a couple of days, showing accumulation of energy in short waves with the instability  
 155 naturally linked to the Hollingsworth problem. They performed a linear analysis of a planar shallow water version of the model  
 156 discretized with the ‘een’ scheme considering a constant background velocity field and a constant Coriolis parameter. Confirming the  
 157 results from [Hollingsworth et al. \(1983\)](#), the shallow water model was shown to be linearly unstable. Interestingly though, the system  
 158 was shown to be stable if the Coriolis parameter was set to zero.

159 Following the analysis of BPT it is possible to show analytically that indeed for a constant basic background velocity and null Coriolis  
 160 parameter the system is neutrally stable. Since this was not explicitly proven in either BPT or [Lazić et al. \(1986\)](#), we describe the proof  
 161 in Appendix A. Also, BPT show how the non-dimensional growth rate ( $\omega_i$ ) of the instability is related to the Coriolis parameter, and  
 162 that it is stronger for larger grid Rossby numbers, and do not show what happens in the case of absence of rotation ( $f_0 = 0$ ). BPT  
 163 normalize the growth rate using the Coriolis parameter, so that the dimensional growth rate is actually  $f_0\omega_i$ . An increase in the grid  
 164 Rossby number, considering a fixed grid and fixed velocity, is related to the decrease of the Coriolis parameter ( $f_0$ ). BPT shows that  
 165 with increasing grid Rossby number the non-dimensional growth rate ( $\omega_i$ ) also increases, but this increase in  $\omega_i$  is small compared  
 166 to the decrease in  $f_0$ . So, in fact, the dimensional growth rate  $\omega_i f_0$  reduces with a reduction of  $f_0$ , even with an increase of the grid  
 167 Rossby number. In the limit, the dimensional growth rate is zero once  $f_0$  is also zero, in agreement with the analysis of Appendix A.

168 This all goes against our intuition about the known source of the instability, which is the lack of discrete cancellation of terms related  
 169 to momentum advection solely. This is elucidated in what follows.

170 The momentum advection plus Coriolis term may be written in vector invariant form as

$$\mathbf{v} \cdot \nabla \mathbf{v} + f \mathbf{k} \times \mathbf{v} = \nabla K + (\zeta + f) \mathbf{k} \times \mathbf{v}, \quad (4)$$

171 where we see that the Coriolis term is added to the vorticity term. The basic velocity states used in both analysis, BPT and [Lazić](#)  
 172 [et al. \(1986\)](#), did not have background vorticity. Following the notation from BPT for the planar analysis, let us impose a non-rotating  
 173 ( $f_0 = 0$ ) system, but add a background basic flow with vorticity as

$$u = u_1 - \zeta_0 y, \quad v = v_1 + \zeta_0 x, \quad (5)$$

174 where  $u_1, v_1$  are constant velocities and  $2\zeta_0$  will be the basic flow vorticity. Assume a constant basic depth,  $\eta_0$ , and let the bottom  
 175 topography ( $b$ ) be used to ensure steady state as

$$gb = gb_0 + \zeta_0(v_1 x - u_1 y) + \frac{\zeta_0^2}{2}(x^2 + y^2), \quad (6)$$

176 where  $g$  is the gravity constant and  $b_0$  is a constant.

177 With this basic state, performing the linear analysis would lead to a set of stability equations that depend on the position  $(x, y)$ .  
 178 By assuming that the disturbances are of small scale compared with that on which the zonal flow varies, that is, that terms involving  
 179 perturbation variables times position variables ( $x$  or  $y$ ) are neglected, this dependence disappears. As a consequence, simple calculations  
 180 show that all that changes in the linear equations derived in BPT is that  $\zeta_0$  appears instead of  $f_0$ . Therefore, the system with  $f_0 = 0$ , but  
 181 with background vorticity  $\zeta_0 \neq 0$ , is unstable and subject to exactly the same analysis as done in BPT for the height coordinate model.  
 182 We clearly see that the Coriolis term is acting as a background vorticity, which seems to be necessary to trigger the instability. Also,

\*European Centre for Medium-Range Weather Forecasts

183 one could interpret the relationships between the Rossby numbers and the instability growth rates simply as Rossby numbers relative  
 184 to the background vorticity of the flow, not necessarily related to the Earth rotation.

185 Summarizing, although the Coriolis term plays no role in the lack of cancellation that leads to the existence of the instability, it can  
 186 influence the instability as a source of vorticity in the vector invariant momentum equations. Also, in the absence of rotation ( $f_0 = 0$ )  
 187 the ‘een’ scheme is still linearly unstable when the background state has non-zero vorticity and varies slowly between grid points.

188 In spherical geometry one cannot define a continuous constant vector field over the whole surface. Therefore, basic states used for  
 189 linear analysis naturally have some source of divergence or vorticity. Simple basic states, such as the purely zonal flows that will be  
 190 defined next in Section 4, should have enough vorticity to trigger the instability even without the Coriolis term.

#### 191 4. Test case

192 In this section we describe a zonal balanced flow test case that mimics small equivalent depth behaviours in spherical shallow water  
 193 models. This will be used to analyse the stability properties of several schemes in later sections. Shallow water models based on  
 194 either non-depth-weighted or depth-weighted Coriolis terms will be considered, as defined in section 2.2. The test is based on existing  
 195 spherical shallow water tests (Williamson *et al.* 1992) and is intended to be very simple to implement in existing codes.

196 Consider as basic state a constant fluid depth  $\eta_0$ , which is used to mimic small equivalent depths and may vary from millimetres to  
 197 a few metres, and a zonal flow ( $u = u_0 \cos(\phi)$ ,  $v = 0$ ), with maximum velocity given by  $u_0 = 2\pi a/12\text{days} \approx 38.6 \text{ ms}^{-1}$ , where  $\phi$  is  
 198 the latitude and  $a = 6.371 \text{ km}$  is the Earth radius.

199 The bottom topography is then used to ensure a steady state,

$$b = \frac{1}{g} \left( a\Omega u_0 + \frac{u_0^2}{2} \right) \sin^2(\phi), \quad (7)$$

200 where  $g = 9.80616 \text{ ms}^{-2}$  is the gravity constant and  $\Omega = 7.292 \times 10^{-5} \text{ rad} \cdot \text{s}^{-1}$  is the rotation rate of the Earth. The test should be  
 201 set up identically as in test case 2 of Williamson *et al.* (1992), except that the topography is used to balance the flow to become steady  
 202 state, and the depth is defined to be constant ( $\eta_0$ ). A good starting point for the constant depth is to assume  $\eta_0 = 1\text{m}$ , but some models  
 203 may require tests with smaller depths. As in the Williamson *et al.* (1992) test cases, all the experiments performed in this study do not  
 204 use any additional perturbation to the initial conditions, as the numerical errors are enough to allow possibly existing unstable modes  
 205 to emerge. Schemes that exactly represent the initial steady state may need a small perturbation in the initial conditions to allow an  
 206 investigation of the unstable modes.

207 For the analysis of the Hollingsworth instability, this test may be ran without the Coriolis term ( $\Omega = 0$ ), since the instability happens  
 208 due to the lack of a discrete cancellation of advection terms solely.

209 The theoretical linear analysis for spherical models can be rather complicated, particularly on unstructured spherical grids. Also,  
 210 numerical implementations of schemes for spherical shallow water models rarely allow the possibility of running linear shallow water  
 211 only. Nevertheless, it is not difficult to numerically investigate the eigen-structure of the most unstable modes with slight modifications  
 212 of a nonlinear shallow water code. In this work, we use a variation of the power method for small perturbations, which is fully described  
 213 in Appendix B.

214 The output of the method is the value of the largest growth rate of a possibly existing unstable mode, which can be used to infer  
 215 the e-folding time (time for the numerical solution to grow by a factor of  $e$ ), and its associated eigenvector, which describes the spatial  
 216 structure of the unstable mode.

#### 217 5. Instabilities on quasi-uniform spherical grids

218 In this section we investigate the stability of spherical shallow water models that adopt the vector invariant form of the momentum  
 219 equations and quasi-uniform spherical grids (Staniforth and Thuburn 2012) considering small equivalent depths.

##### 220 5.1. Analysis of Finite Volume schemes on icosahedral grids

221 For recently developed schemes that use spherical unstructured grids, it is very difficult to derive formulations in which the advection  
 222 term is decomposed into vortical and kinetic energy terms in a way that satisfies the cancellation property in the discrete sense.  
 223 Considering mimetic finite volume schemes for hexagonal-pentagonal grids (Voronoi grids), following the discretizations proposed in  
 224 (Thuburn *et al.* 2009; Ringler *et al.* 2010), hereafter named TRSK, no discrete cancellation is expected and the model is prone to being  
 225 unstable. Shallow water experiments with TRSK on the sphere (Ringler *et al.* 2010; Weller *et al.* 2012; Peixoto 2016) did not reveal  
 226 instabilities related to the non-cancellation issue of the vector invariant momentum equations. Nevertheless, Skamarock *et al.* (2012)  
 227 and Gassmann (2013) show that the instability indeed appears in 3D models. We will show here that the main point for the instability  
 228 not to appear in the shallow water models was that the growth rates of the instability were too small because of the large fluid depths  
 229 adopted and runtime scales tested.

230 TRSK is well suited for icosahedral grid-based models. Icosahedral grids can be initially built based on a triangulation of the sphere  
 231 (a Delaunay grid), but usually the dual grid (its Voronoi diagram) is adopted for the finite volume computational cells (Staniforth and  
 232 Thuburn 2012). All test cases here use a dual Voronoi (hexagonal-pentagonal) grid of level 5, that has 10242 computational cells (12  
 233 regular pentagons and 10230 not necessarily regular hexagons) which corresponds to an approximate grid resolution of 240km. This  
 234 resolution may not adequately resolve the Rossby radius of deformation in most experiments performed below, but it is fine enough to  
 235 investigate the stability of the scheme in a non-time-consuming way. See section 5.3 below for further discussion of this point.

236 The grids used here adopt a Spherical Centroidal Voronoi Tessellation (SCVT), which slightly modifies the original icosahedral grid  
 237 cell nodes to ensure that they are very close to the centroid of the Voronoi cell that they define (Ju *et al.* 2011). In what follows, all  
 238 figures that show spatial distribution of a scalar field on this grid will also show the Voronoi diagram associated with the basic triangular

239 icosahedral grid, to serve as reference of the underlying grid structure. A four stage, fourth order, explicit Runge-Kutta was used as the  
 240 time-stepping scheme with a time-step of 400s.

241 The original TRSK scheme is proposed to ensure total energy conservation (within time truncation error) and compatibility with the  
 242 potential vorticity equation. To achieve this, the vorticity terms are weighted by the layer depth. We start the analysis with this original  
 243 depth-weighted (DW) formulation and later show how the scheme behaves with a non-depth-weighted (NDW) formulation, which  
 244 should be more closely related to the results of [Skamarock \*et al.\* \(2012\)](#) and [Gassmann \(2013\)](#), since they adopt level-based vertical  
 245 coordinate systems.

#### 246 Zonal balanced flow with no Coriolis force for depth-weighted TRSK

247 We start the analysis with the zonal balanced flow described in section 4, but without the Coriolis force ( $\Omega = 0$ ), just to illustrate  
 248 that indeed the Hollingsworth instability can be triggered independently of a Coriolis force. Using the original TRSK scheme (depth-  
 249 weighted) and a constant fluid depth of 1 m, the model is unstable and the linear analysis shows that the most unstable mode has a  
 250 growth rate with e-folding time of 25.7 days, and eigenvector shown in Figure 1. We see that the mode is related to the underlying grid  
 251 structure. For a depth of 0.1 m the e-folding time reduces to 19.5 days, and for a depth of 0.01 m the e-folding time drops to 5.2 days.  
 252 For large depths, such as 100 m or larger, the model does not blow up in run-times of up to one year.

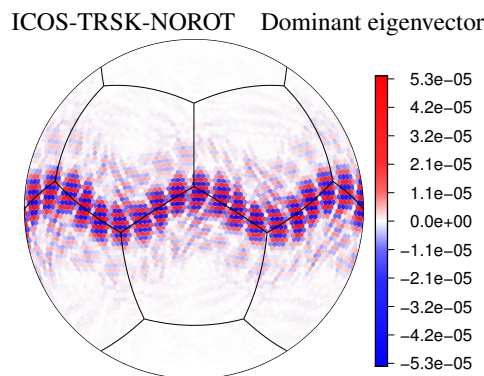


**Figure 1.** Dominant eigenvector for the depth field deviation from basic state with constant mean depth of 1 m for the TRSK scheme considering the zonal flow test case without Coriolis force.

253 This example shows how the Hollingsworth instability exists independently of the Coriolis force. Nevertheless, since most  
 254 atmosphere and ocean models do have the Coriolis term included, we will continue with further analysis using only the test with  
 255 Coriolis force included.

#### 256 Zonal balanced flow with Coriolis force for depth-weighted versions of TRSK

257 We will now consider the test of balanced zonal flow with rotation, as described in section 4. Adopting a constant fluid depth of 1 m, we  
 258 show in Figure 2(a) the error in the depth field for the TRSK scheme after 14.5 days, which is a few time steps before the model blows  
 259 up. The model is clearly unstable and Figure 2(b) shows the dominant eigenvector. Both the error and the eigenvector patterns seem to  
 260 be related to geometric properties of the grid, which agrees with previous knowledge of grid imprinting often observed in this kind of  
 261 model ([Peixoto and Barros 2013](#); [Weller \*et al.\* 2012](#)), but they do not match each other exactly. The method used for the linear analysis  
 262 is sensitive to possibly very close eigenmodes, which may be hard to separate. Also, nonlinear effects may influence the patterns in the  
 263 full model run. Nevertheless, both patterns seem to indicate that the unstable mode is stronger near edges of the original icosahedral  
 264 dual grid.

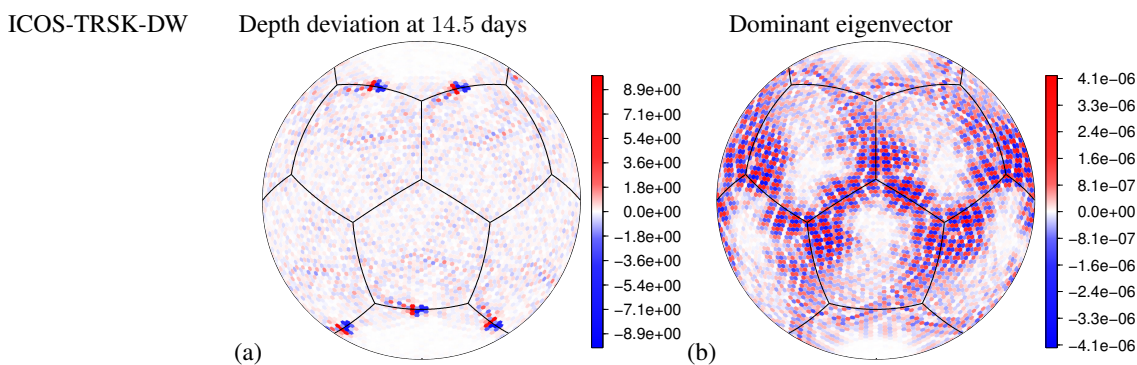


**Figure 2.** (a) Depth field deviation from a basic state with mean depth of  $\eta_0 = 1$  m for the depth-weighted TRSK scheme at time 14.5 days considering the zonal flow test case with Coriolis terms. The stopping time is a few time-steps only from blow-up. (b) Dominant eigenvector for the depth field deviation from basic state with constant mean depth of 1 m.

265 The blue line in Figure 3, referring to the TRSK scheme, shows the e-folding times of the instability for various depths. The instability  
 266 is noticeably stronger for the smaller the depths, almost reaching an e-folding time of approximately 1 day. For the depths adopted in  
 267 standard shallow water test cases ([Williamson \*et al.\* 1992](#)), which are of about 10km, the growth rate is so small that one would not  
 268 observe instabilities even in long runs (of many years). For the high resolution 3D models discussed in section 2, which have very small

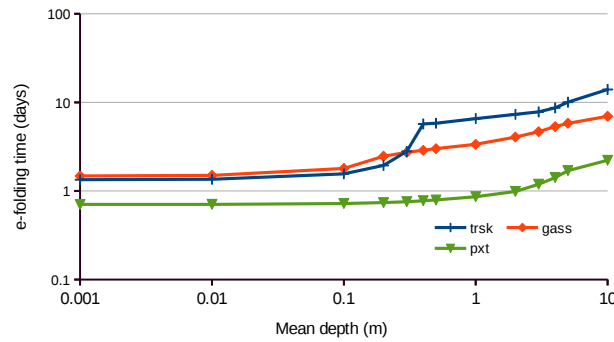


Figure 3. E-folding times (days) for different mean fluid depths ( $\eta_0$ ) and different finite volume schemes with depth-weighted vorticity terms (TRSK, GASS and PXT).

269 equivalent depths, we are very likely to be in the region where the e-folding time is near to 1 day. This can have significant impact in  
 270 medium- and long-range weather forecasts, and also in long climate simulations for either the ocean or the atmosphere.

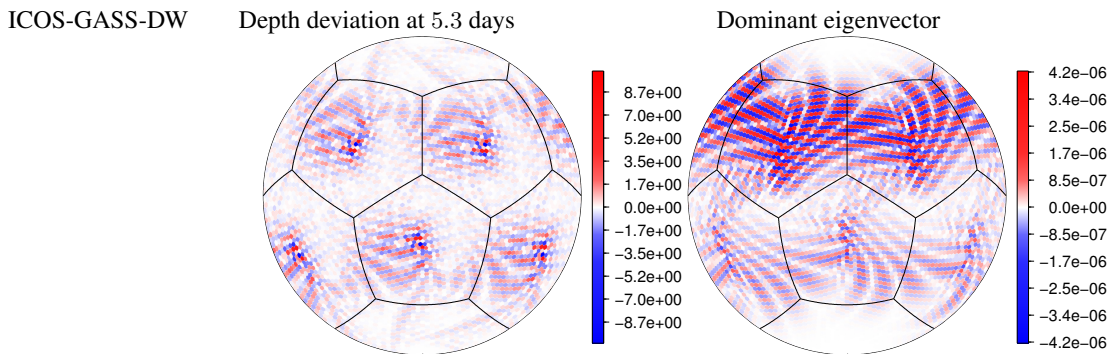


Figure 4. Same as Figure 2, but now for the GASS scheme with depth-weighted vorticity, and error at time 5.3 days.

271 Gassmann (2013) analysed the instability problem on planar regular hexagons and did not find a way to modify the kinetic  
 272 energy discretization to ensure exact discrete cancellation. Nevertheless, a discretization that minimizes the non-cancellation effect  
 273 is suggested. In 3D models this scheme was shown to reduce the effects of the instability in standard baroclinic wave test cases (e.g.  
 274 Skamarock *et al.* 2012; Gassmann 2013). The stable results observed are of course very important to enable practical usage of such  
 275 schemes, but no warranty of stability is established. In fact, it might be the case that other experiments, or longer run-time periods,  
 276 reveal the instability.

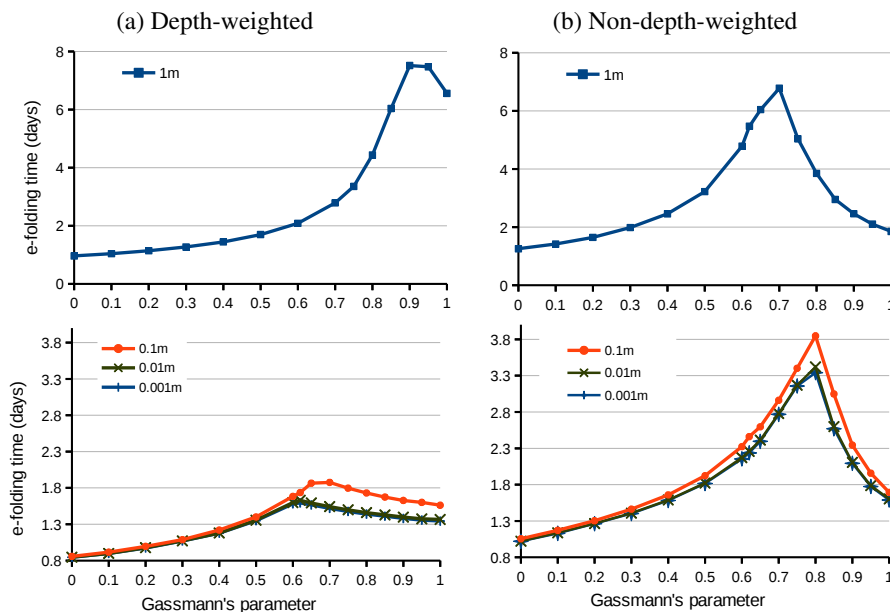


Figure 5. E-folding time (days) relative to different parameter choices ( $\alpha$ ) of GASS scheme with constant mean depths of 1 m (top), 0.1 m, 0.01 m and 0.001 m (bottom). On the left (a) for depth-weighted vorticity, on the right (b) for non-depth-weighted vorticity.

277 We examined the scheme proposed by Gassmann (2013) (hereafter denoted as GASS scheme) using the the zonal flow test case with  
 278 Coriolis force. Considering 1 m constant depth, it blows up shortly after 5 days. Figure 4(a) shows the error in the depth field a few steps  
 279 before blowing up. The errors dominate at the center of the original pentagons of the icosahedral grid, so they are clearly connected  
 280 to the grid structure. The linear analysis of this scheme, confirms the lack of stability, and the pattern of the dominant eigenvector is

281 given in Figure 4(b) and also shows larger values near the center of the original pentagons. We notice that the blow-up time in this case  
 282 was sooner than that of the original TRSK scheme. This is confirmed by the calculation of the e-folding time, which is smaller for the  
 283 GASS scheme (see Figure 3 for 1 m depth).

284 The above result is somewhat counter-intuitive compared with the previous results discussed by Skamarock *et al.* (2012) and  
 285 Gassmann (2013) for 3D models, since in this scenario the modification seems to have worsened the stability of the scheme. There are  
 286 two main points here. First, these 3D models can be more naturally classified as having non-depth-weighted vorticity terms, since the  
 287 vorticity is weighted by density, not the layer depth. A non-depth-weighted version of the TRSK scheme will be investigated later in  
 288 this paper. Also, both models use a Lorenz vertical grid, which, as discussed in section 2, is related to very small equivalent depths  
 289 (much smaller than the 1 m tested here). For smaller equivalent depths, the GASS scheme has e-folding time larger than the original  
 290 TRSK scheme, as one can see in Figure 3, noting that the two lines cross at about half metre. For example, for a depth of 0.1 m, TRSK  
 291 has e-folding of 1.56 days and GASS has 1.8 (the growth rate is approximately 15% slower with GASS scheme).

292 The modified kinetic energy proposed by Gassmann (2013) is based on a linear combination of the original kinetic energy used  
 293 in TRSK, defined at cell centers and which we will denote as  $K_c$ , and a kinetic energy  $K_v$ , calculated based on the kinetic energies  
 294 obtained from the triangles surrounding the cell, which results in the total kinetic energy  $K = \alpha K_c + (1 - \alpha)K_v$ . The choice of  $\alpha = 1$   
 295 gives back the original TRSK scheme, and a standard choice of  $\alpha = 0.75$  is suggested to be stable, as it minimizes the cancellation  
 296 error in the advection decomposition on the plane. The experiments shown so far all adopted this standard parameter of  $\alpha = 0.75$ . Now  
 297 we investigate the influence of this parameter choice with respect to the growth rates of the most unstable modes. Figure 5(a) shows  
 298 how the e-folding times vary with  $\alpha$  for four choices of equivalent depths. For a depth of 1 m, we notice that the choice of parameter  
 299 of  $\alpha = 0.75$  seems to give faster growth rates (smaller e-folding times) than the original scheme (as already observed before), but the  
 300 figure also points out that it is possible to choose the parameter in a range that reduces the growth rates ( $\alpha$  near 0.9 – 0.95). For a  
 301 smaller depth, of 0.01 m, the scheme using  $\alpha = 0.75$  indeed gives smaller growth rates, but the optimal parameter in this case would  
 302 be close to  $\alpha = 0.625$ , which is in fact what is adopted in the MPAS<sup>†</sup> model (Skamarock *et al.* 2012). Experiments with even smaller  
 303 depths seems to indicate that the choice of  $\alpha = 0.625$  is optimal for very small equivalent depths.

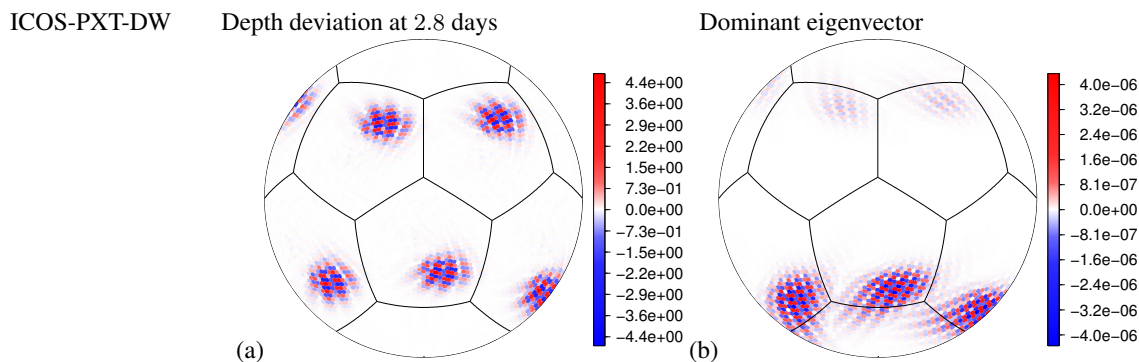


Figure 6. Same as Figure 2, but now for the PXT scheme with depth-weighted vorticity, and error at time 2.8 days.

304 Peixoto (2016) noticed that the gradient of the kinetic energy discretization used in the TRSK scheme was very inaccurate on  
 305 unstructured spherical grids, in fact, it was proven to be inconsistent (0th order accurate), a problem also shared with the discretization  
 306 of other terms of the TRSK scheme. Peixoto (2016) suggests modifications of the TRSK scheme to ensure at least overall first order  
 307 accuracy, at the cost of losing some mimetic properties. More accurate kinetic energy and vorticity discretizations could, in theory,  
 308 reduce the mis-cancellation gap that occurs in the advective term. The cancellation in this case would be ensured asymptotically for  
 309 sufficiently smooth fields. Nevertheless, stability issues are usually related to near-grid-scale features, so asymptotic cancellation might  
 310 not be enough to avoid the instability. We investigated the stability of the consistent scheme proposed in Peixoto (2016), which we  
 311 hereafter refer to as PXT. The test case using 1 m depth shows that the scheme blows up shortly before 3 days (see Figure 6(a) for the  
 312 pattern of the error in the depth field at 2.8 days). The growth rate is in fact somewhat larger than that of the original TRSK scheme, as  
 313 illustrated by the smaller e-folding times in Figure 3 with label PXT.

#### 314 Analysis of non-depth-weighted versions of TRSK

315 So far, all analysis done for the TRSK-based schemes has considered the depth-weighted form of the vorticity term, as in the original  
 316 shallow water formulation, and appropriate for a three-dimensional layer-based coordinate model. It is possible to remove the depth  
 317 weighting of the vorticity, corresponding to a three-dimensional level-based coordinate, although some mimetic properties will be lost.

318 We analysed the non-depth-weighted version of TRSK and found it to be unstable. The error pattern of the depth field observed a  
 319 few steps before blow-up assuming a mean depth of 1 m is shown in Figure 7. The calculated growth rate indicates an e-folding time  
 320 of 1.85 days, which is smaller than the e-folding time of the layer version of TRSK (which has an e-folding time of approximately 6.5  
 321 days), so the instability grows faster in the non-depth-weighted version for this mean depth.

322 The GASS scheme can also be used without depth weighting of the vorticity term. In fact, the method as derived in Gassmann  
 323 (2013) considered only the relative vorticity, not the potential vorticity. Also, in three-dimensional models such as MPAS (Skamarock  
 324 *et al.* 2012), the vorticity is weighted by density rather than the fluid layer depth, and the behaviour is best captured by the non-depth-  
 325 weighted shallow water case. The non-depth-weighted version of the GASS scheme, using the original scheme parameter choice of  
 326 0.75, is still unstable, with e-folding times shown in Figure 5(b). With a mean fluid depth of 1 m, the e-folding time of the instability is  
 327 approximately 5 days, so this time larger than the original TRSK scheme. For a smaller depth of 0.01 m we have an e-folding time of

<sup>†</sup>The Model for Prediction Across Scales (MPAS)



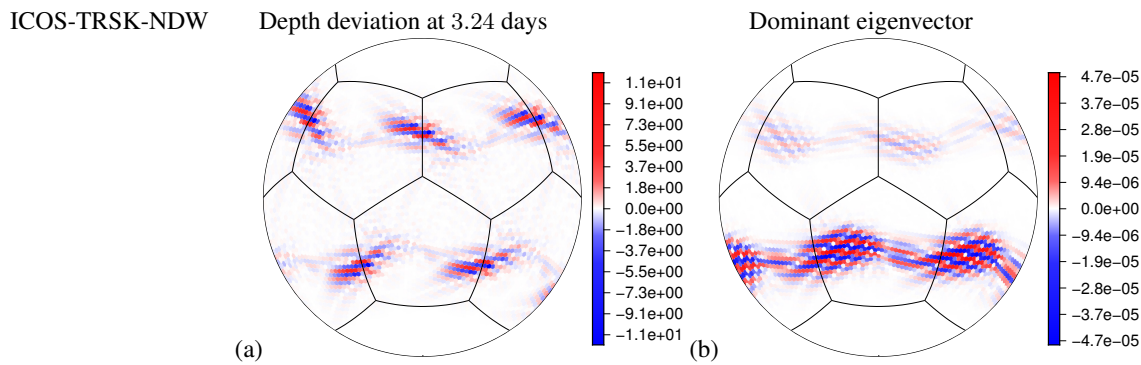


Figure 7. Same as Figure 2, but now for the non-depth-weighted TRSK scheme and error at time 3.24 days.

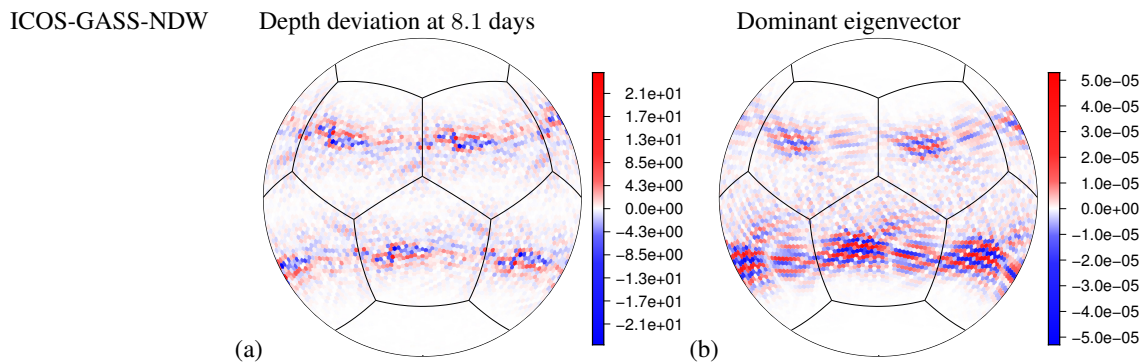


Figure 8. Same as Figure 2, but now for the non-depth-weighted GASS scheme and error at time 8.1 days.

328 1.6 days for TRSK and 3.2 days for GASS. Therefore the GASS scheme seems to be slowing down the growth speed of the instability  
 329 with respect to TRSK.

330 We show in Figure 5(b) how the parameter choice of the GASS scheme affects the e-folding time of the most unstable mode. In all  
 331 our tests with the non-depth-weighted scheme, using the GASS scheme with the original parameter choice of 0.75 was always beneficial  
 332 to reduce the growth speed of the instability. We also note that the modification of the GASS scheme seems to be more effective (larger  
 333 e-folding times) for the non-depth-weighted scheme than for the depth-weighted scheme when compared to the original TRSK scheme  
 334 (the TRSK scheme e-folding times can be observed in the same figure looking at the parameter choice of 1).

335 As a result from the shallow water equation analysis for both depth-weighted and non-depth-weighted models, we conclude that  
 336 the modification proposed by Gassmann (2013) does not seem to be enough to eliminate the instability. Nevertheless, it can delay its  
 337 interference in the model by reducing its growth rate. The two 3D models for which the instability was recently reported (Skamarock  
 338 *et al.* 2012; Gassmann 2013) showed results based on a baroclinic wave test suggested by Jablonowski and Williamson (2006). The  
 339 tests show a clear unstable mode at day 8 or 9 of integration for the original TRSK scheme. At day 9, Gassmann's scheme does not  
 340 reveal traces of the unstable mode yet. From our analysis, apparently the instability has not yet grown significantly, due to the smaller  
 341 growth rate, but it is prone to appear in later times. Further investigations to see if indeed the instability appears later in the baroclinic  
 342 wave test case would be required to confirm the extension of these results for 3D models, but this is beyond the scope of this paper.

## 343 5.2. Analysis of a Finite Element Mimetic scheme

344 Thuburn and Cotter (2015) proposed a finite element numerical scheme for the shallow water equations on a rotating sphere. It uses  
 345 compound elements, which provide a generalization of the lowest order Raviart-Thomas finite elements to arbitrary polygonal grids  
 346 and give a finite element analogue of the C-grid placement of variables. The finite element scheme is closely related to the finite volume  
 347 scheme of Thuburn *et al.* (2014), which in turn is derived from TRSK. It has the same mimetic properties, and it uses the same semi-  
 348 implicit time integration scheme and the same finite volume advection scheme for advection of mass and potential vorticity. As in the  
 349 original TRSK scheme, this finite element scheme also adopts a depth-weighted vorticity in order to obtain compatibility between the  
 350 linear shallow water equation scheme and the discrete potential vorticity equation. The finite element scheme has greater accuracy than  
 351 TRSK, which comes at the price of inverting certain mass matrices and related operators at each time step.

352 The discretizations are built starting from the vector invariant form of the equations, and so are susceptible to non-cancellation  
 353 effects of the momentum advection term decomposition. No numerical instabilities were detected within the experiments performed in  
 354 the original paper. Closely related numerical methods are under consideration for the next generation three-dimensional atmospheric  
 355 dynamical core at the UK Met Office. Therefore, insights about whether the Hollingsworth instabilities will happen in this case are  
 356 highly desirable.

357 We used our suggested test case of a very thin layer of shallow water (with Coriolis force) to investigate potential instabilities. Two  
 358 grid possibilities were used: (i) a cubed sphere grid, where we used a resolution with 13824 quadrilateral cells, and (ii) an icosahedral  
 359 based grid, formed by hexagons and 12 pentagons, where we used a resolution with 10242 Voronoi cells. The icosahedral grid was  
 360 modified with the approach suggested by Heikes and Randall (1995), and has an orthogonal dual grid, whereas the cubed sphere grid  
 361 used the same modification adopted in Thuburn *et al.* (2014), and is non-orthogonal. The time step adopted was 400 s.

362 Our experiments showed that the model indeed reveals itself to be unstable under small enough mean fluid depth. For a mean depth  
 363 of 1 m, the cubed sphere model blows up shortly after 5.17 days (see Figure 9(a)). For this same depth, the hexagonal grid did not blow

364 up for runs of over one year, which shows that it is potentially less susceptible to the instability. Nevertheless, for a mean depth of  
 365 0.10 m, it blows up shortly after 5.95 days (see Figure 9(a)).

366 An attempt to use the power method to estimate the growth rates was performed. We observed lack of convergence of the algorithm  
 367 in the experiments performed, even with very small mean depths. The dominating vector seems to be strongly caught by grid structures  
 368 during the iterations, and does not seem to reflect the actual dominant computational mode of the instability. So these results are not  
 369 shown.

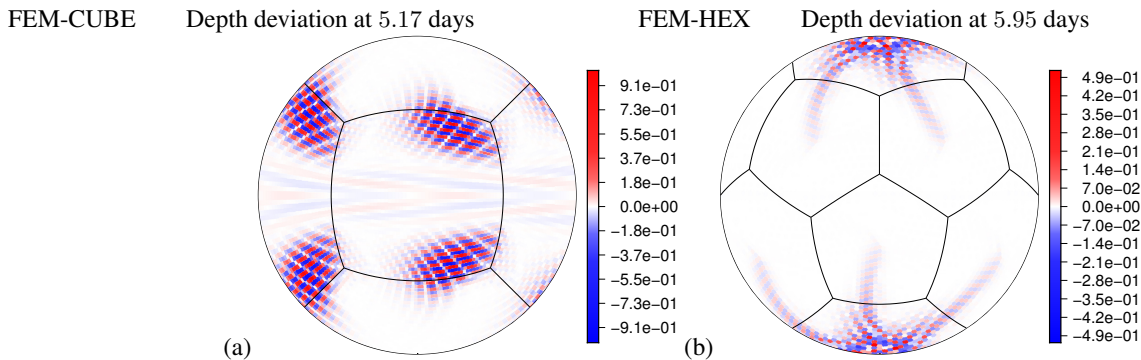


**Figure 9.** (a) Depth field deviation from basic state considering a constant mean depth of  $\eta_0 = 1$  m for the FEM scheme on a cubed sphere at time 5.17 days. (b) Depth field deviation from basic state considering a constant mean depth of  $\eta_0 = 0.1$  m on an icosahedral grid at time 5.95 days.

### 370 5.3. Equivalent depths and the Rossby radius of deformation

371 In the experiments discussed above, reducing the mean depth has the effect of reducing the Rossby radius of deformation  $\lambda = \sqrt{g\eta_0}/f$ .  
 372 It is well-known that C-grid schemes can behave poorly when the Rossby radius is not well resolved. For example, taking  $\eta_0 = 1$  m,  
 373 the Rossby radius at mid-latitudes is approximately  $\lambda = \sqrt{g\eta_0}/f \approx 30$  km, which is far from being resolved on the grids used above  
 374 with horizontal resolution of approximately 240 km. It is therefore legitimate to ask whether the poor resolution of the Rossby radius  
 375 might be contributing to the observed instability, and whether the instability might be ameliorated by using much higher horizontal  
 376 resolution typical of that in modern weather and climate models.

377 For the non-depth-weighted ‘een’ and ‘AL’ schemes on a plane, the analysis of BPT (their figures 6 and 7) shows that the growth  
 378 rate (non-dimensionalized using  $f$ ) in fact increases as resolution is refined, that is, for increasing grid Rossby number  $R_u$  keeping  
 379 Froude number  $F_u$  fixed. Consistent with this, [Ducouso et al. \(2017\)](#) found that, in a version of the NEMO ocean model using the  
 380 ‘een’ scheme, the instability became significantly worse at finer horizontal resolution.

381 To examine this issue in our experiments the test cases for depth-weighted TRSK without and with Coriolis force at  $\eta_0 = 1$  m may  
 382 be compared. In the case without Coriolis force, the Rossby radius, based on the the mid-latitude absolute vorticity rather than  $f$ , is  
 383  $\lambda \approx 360$  km and so is marginally resolved. In the case with Coriolis force, on the other hand, the Rossby radius  $\lambda \approx 30$  km is badly  
 384 underresolved. The respective e-folding times are 25.7 days and 6.5 days. Thus, the absolute growth rate of the instability is greater  
 385 for the case of badly underresolved Rossby radius. However, the background absolute vorticity is 13 times as strong in the case with  
 386 Coriolis force. Therefore, the growth rate non-dimensionalized by the background absolute vorticity is in fact greater for the case of  
 387 marginally resolved Rossby radius.

388 We also repeated the test for depth-weighted TRSK, with  $\eta_0 = 1$  m and including Coriolis force, on grids with 120 km, 60 km,  
 389 and 30 km resolution. In all cases the model crashed after about 14.5 days, similar to the original 240 km run. The linear analysis  
 390 indicates that the e-folding time at 240 km resolution is about 6.5 days. Increasing the grid resolution to 120 km and 60 km results  
 391 in e-folding times respectively of 7.4 and 9.5 days. In this set of experiments the growth rate of the instability (both absolute and  
 392 non-dimensionalized) shows a modest decrease as the resolution of the Rossby radius improves.

393 From this limited set of results it appears that the dependence of the instability on resolution of the Rossby radius may be quite  
 394 complicated, and might be affected by the specific scheme used, depth-weighting, spherical geometry, and whether the background  
 395 vorticity is provided by the flow or the planetary rotation. Nevertheless, it is clear that increasing the horizontal resolution does not,  
 396 in general, suppress the instability, and may make it worse. The results also imply that a relatively coarse and computationally cheap  
 397 horizontal resolution, as used in most of our tests, is adequate for diagnosing the presence of an instability.

## 398 6. Analysis of instabilities in ENDGame

399 The discretization of the atmosphere dynamical core of the Unified Model of the UK MetOffice, also known as ENDGame ([Wood  
 400 et al. 2014](#)), is based on the shallow water discretization discussed in [Zerroukat et al. \(2009\)](#). In this section, we will first perform a  
 401 linear stability analysis of the [Zerroukat et al. \(2009\)](#) scheme and two alternatives, under a similar approach as adopted in BPT, for the  
 402 planar version of the scheme. This shows that depth weighting of the Coriolis term on its own can give rise to instabilities, depending  
 403 how it is applied. Then, we will show numerical results for the spherical shallow water model. Implications for the stability of the  
 404 three-dimensional ENDGame will be discussed at the end.

405 6.1. Analysis on an  $f$ -plane

## 406 6.1.1. Original ENDGame scheme

Following the notation of BPT, consider the shallow water equations written in advective form for a planar domain with velocity components  $(u, v)$ , water height  $\eta$  and bottom topography (bathymetry)  $b$ ,

$$\begin{aligned} u_t + uu_x + vv_y - f_0v &= -g(\eta_x + b_x), \\ v_t + uv_x + vv_y + f_0u &= -g(\eta_y + b_y), \\ \eta_t + (u\eta)_x + (v\eta)_y &= 0, \end{aligned} \quad (8)$$

407 where the subscripts refer to partial derivatives,  $g$  is the gravity constant,  $f_0$  is the Coriolis parameter (constant) and the free surface  
408 height is given by  $\eta + b$ .

The scheme proposed in [Zerroukat et al. \(2009\)](#) adopts a semi-implicit semi-Lagrangian approach, but we are interested in the instabilities that arise due to spatial discretizations related to geostrophic and inertia-gravity linear modes, so we will adopt a simplified advection scheme. The scheme is constructed on a usual horizontal C-staggered grid. The semi-discrete version of these equations for a planar domain of constant Coriolis parameter can then be written as

$$\begin{aligned} u_t + u\delta_x\overline{u^x} + \overline{v^x}\delta_y\overline{u^y} - \frac{f}{\eta}\overline{\overline{\eta^y}v^y} &= -g(\delta_x\eta + \delta_x b), \\ v_t + \overline{u^y}\delta_x\overline{v^x} + v\delta_y\overline{v^y} + \frac{f}{\eta}\overline{\overline{\eta^x}u^x} &= -g(\delta_y\eta + \delta_y b), \\ \eta_t + \delta_x(u\overline{\eta^x}) + \delta_y(v\overline{\eta^y}) &= 0, \end{aligned} \quad (9)$$

409 where the over-lines indicate a centred averaging in the direction of the super-script and the  $\delta$ s indicate a centred differencing in the  
410 direction of the sub-script (see BPT for details on the notation). The key point of this discretization is that it uses depth-weighted  
411 Coriolis terms so that the Coriolis terms do not contribute to the energy budget and have good Rossby mode dispersion properties  
412 ([Thuburn and Staniforth 2004](#)).

413 The linearization will be taken with respect to a geostrophically balanced non-resting steady state. To ensure the flow is balanced,  
414 one could either think of adding a forcing to the equations, or else, and as we will adopt, use the bottom topography  $b$  to enforce the  
415 steady state. To do so, consider the constant basic velocity and mean water depth,  $(u_1, v_1, \eta_0)$ , and bottom topography defined as

$$b = b_0 + \frac{f_0}{g}(v_1x - u_1y), \quad (10)$$

416 with  $b_0$  constant. Clearly the bottom topography terms in the right-hand-side of the discrete equations reduce to  $f_0v_1$  and  $-f_0u_1$  for  
417 the  $u$  and  $v$  equations, respectively.

The linearized version of these equations may then be written for the perturbations variables ( $u' = u - u_1, v' = v - v_1, \eta' = \eta - \eta_0$ )  
as

$$\begin{aligned} u'_t + u_1\delta_x\overline{u'^x} + v_1\delta_y\overline{u'^y} - f_0\overline{v'^xy} - \frac{f_0v_1}{\eta_0}(\overline{\overline{\eta'^yy}} - \eta'^x) &= -g\delta_x\eta', \\ v'_t + u_1\delta_x\overline{v'^x} + v_1\delta_y\overline{v'^y} + f_0\overline{u'^xy} + \frac{f_0u_1}{\eta_0}(\overline{\overline{\eta'^xx}} - \eta'^y) &= -g\delta_y\eta', \\ \eta'_t + \eta_0(\delta_x u' + \delta_y v') + u_1\delta_x\overline{\eta'^x} + v_1\delta_y\overline{\eta'^y} &= 0, \end{aligned} \quad (11)$$

418 where the over-lines with double superscript indicates averaging in both directions indicated.

419 Assume that the perturbations are of a wave-like form,

$$(u', v', \eta') = (\hat{u}, \hat{v}, \hat{\eta})\exp\left(\frac{i\kappa x}{\Delta x} + \frac{i\lambda y}{\Delta y} - i\omega f_0 t\right), \quad (12)$$

420 where  $\omega$  is a non-dimensional frequency normalised using  $f_0$ , and  $\kappa$  and  $\lambda$  are non-dimensional horizontal wavenumbers for the  $x$ - and  
421  $y$ -directions normalised using the grid spacings  $\Delta x$  and  $\Delta y$  respectively. Define the following convenient non-dimensional quantities

$$F_u = \frac{u_1}{c}, \quad F_v = \frac{v_1}{c}, \quad R_c = \frac{2c}{f_0\Delta y}, \quad X = \frac{\Delta x}{\Delta y}, \quad (13)$$

422 respectively for the Froude numbers for the basic flows  $u_1$  and  $v_1$ ,  $R_c$  as twice the ratio of the Rossby radius ( $c/f_0$ ) and the grid spacing  
423  $\Delta y$ , where

$$c = \sqrt{g\eta_0}. \quad (14)$$

424 The grid-scale Rossby numbers  $R_u$  and  $R_v$  for the flows  $u_1$  and  $v_1$  can be constructed using the above parameters

$$R_u = \frac{2u_1}{f_0\Delta x} = \frac{F_u R_c}{X}, \quad R_v = \frac{2v_1}{f_0\Delta y} = F_v R_c. \quad (15)$$

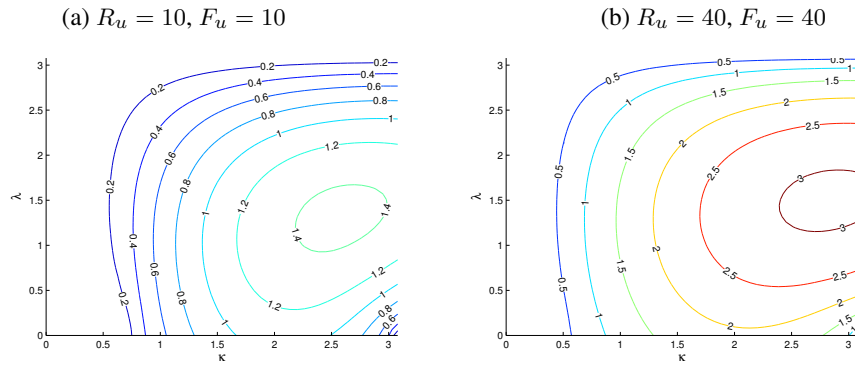


**Figure 10.** The fastest growing instabilities (maximum  $|\omega_i|$ ) for varying  $\lambda$  and  $\kappa$  for the ENDGame scheme for the case with  $v_1 = 0$  and two combinations of  $R_u$  and  $F_u$ .

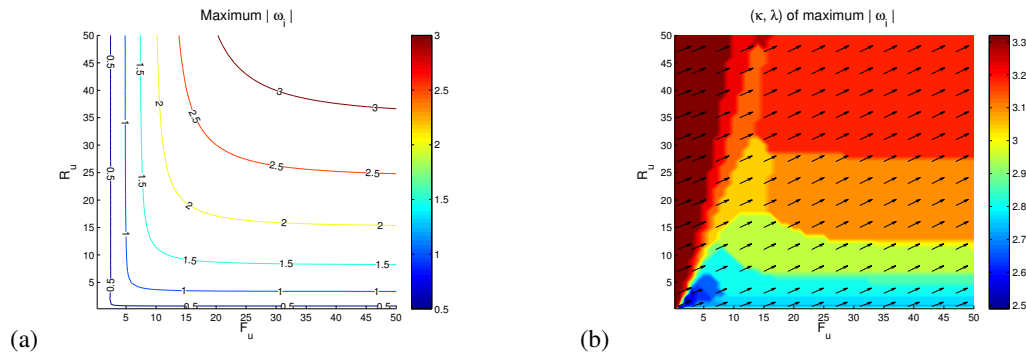


**Figure 11.** The fastest growing instabilities for all  $\lambda$  and  $\kappa$  for the ENDGame scheme for the case with  $v_1 = 0$  as a function of  $F_u$  and  $R_u$ ; (a) the maximum non-dimensional growth rates,  $|\omega_i|$ , and (b) their wavenumber ( $\kappa, \lambda$ ); the arrows show their direction and the contours their magnitude.

425 Substituting the wave-like form into the discrete linearized equations (11), and using the above relations together with the definitions,  
426

$$c_p = \cos(p/2), \quad s_p = \sin(p/2), \quad p = \kappa, \lambda, \quad (16)$$

one obtains a matrix form of the stability problem,

$$\begin{bmatrix} \varpi & -i c_\kappa c_\lambda & -\frac{R_c s_\kappa}{X} - i E_u \\ i c_\kappa c_\lambda & \varpi & -R_c s_\lambda + i E_v \\ -\frac{R_c s_\kappa}{X} & -R_c s_\lambda & \varpi \end{bmatrix} \begin{bmatrix} \hat{u} \\ \hat{v} \\ \frac{c\hat{\eta}}{\eta_0} \end{bmatrix} = 0, \quad (17)$$

where

$$\begin{aligned} \varpi &= \omega - R_u s_\kappa c_\kappa - R_v s_\lambda c_\lambda, \\ E_u &= F_v c_\kappa (c_\lambda^2 - 1), \\ E_v &= F_u c_\lambda (c_\kappa^2 - 1). \end{aligned} \quad (18)$$

427 Although it is possible to derive analytical solutions for special cases, such as those aligned with the grid ( $\kappa = 0$ ), these do not  
428 capture the most unstable modes, so direct numerical evaluations of the eigenvalues ( $\omega$ ) of the stability matrices were performed. We  
429 considered only the imaginary part of the eigenvalues,  $\omega_i$ , which is the part that leads to the instability, and present their maximum  
430 absolute values for a few parameter settings in Figures 10 and 11. These show that for a zonal flow ( $v_1 = 0$ ) there are unstable modes  
431 that are stronger for larger horizontal wavenumbers ( $\kappa$ ). The maximum growth rate increases as equivalent depth decreases (increasing  
432 Froude number) and also as horizontal resolution is refined (increasing grid Rossby number). Figure 11(b) shows that the most unstable  
433 modes are not necessarily aligned with the grid.

434 Therefore, the planar version of the ENDGame formulation of the SWEs may suffer from grid-scale instabilities. However, in  
435 comparison to BPT, their dispersion relation is not the same as that for Hollingsworth instabilities; in fact, as will be shown below, it is  
436 solely related to the discretization of the Coriolis term.

### 437 6.1.2. Alternative simplified scheme

438 The instability detected in the previous section is directly related to the form of discretization of the Coriolis term. This can be seen by  
439 noting that if the terms  $E_u$  and  $E_v$  in (17) were set to zero then the matrix of the system could be written as  $(\varpi I + H)$ , where  $H$  is  
440 Hermitian;  $\varpi$  would then be real-valued and the problem is neutrally stable. The terms  $E_u$  and  $E_v$  arise from the the last terms on the  
441 left hand sides of the  $u'$  and  $v'$  equations in (11), which in turn arise from the depth weighting of the Coriolis term.

442 With this insight, it is simple to derive a stable discretization for this problem. For example, using simple uniform averaging

$$fv \approx f\bar{v}^{xy}, \quad fu \approx f\bar{u}^{yx}, \quad (19)$$

443 results in  $E_u = 0$ ,  $E_v = 0$ , and the scheme is then stable for this problem.

444 This is not a new scheme, in fact, it is actually the standard kind of discretization one would first apply in finite difference C-grid  
445 models. It was frequently used in the early days of weather forecasting (e.g. McDonald and Bates 1989) and is still considered in  
446 some models (e.g. Barros and Garcia 2004). Nevertheless, this approach lacks some important properties of the scheme adopted in  
447 ENDGame. For example, in this scheme the Coriolis term is not neutral in the energy budget when used in a layer-based model. On an  
448  $f$ -plane, Eq. (19) is obtained from Eq. (9) simply by removing the depth weighting.

### 449 6.1.3. Alternative energy conserving scheme

450 Alternatively, one can build a depth-weighted discretization that still retains an energy conserving Coriolis term and is stable for the  
451 planar analysis:

$$fv \approx \frac{\overline{f \overline{\eta^y v^x}}}{\overline{\eta^{xy}}}, \quad fu \approx \frac{\overline{f \overline{\eta^x u^y}}}{\overline{\eta^{xy}}}. \quad (20)$$

452 This is identical to the energy conserving scheme of Sadourny (1975), with the exception that here only the planetary vorticity (Coriolis  
453 parameter) is used instead of the absolute or relative fluid vorticity, since the momentum equations are not in vector invariant form.  
454 With this discretization, again it is possible to show that  $E_u = 0$  and  $E_v = 0$ , so the scheme is neutrally stable.

455 One intellectually satisfying aspect of this discretization is that  $f$  is evaluated at vorticity points, which feels more natural and is  
456 closer to the approach of Arakawa and Lamb (1981) than the original scheme, which evaluates  $f$  at mass/pressure points.

## 457 6.2. Analysis on the sphere

### 458 6.2.1. Description of the schemes

459 We have described 3 numerical schemes so far. First the original ENDGame scheme, described in Eq. (9), which we will denote as  
460 ‘‘ORIG’’. Second, the simplified scheme, described in Eq. (19), which we will denote as ‘‘SIMP’’. And third, an alternative energy  
461 conserving scheme, analogous to Sadourny’s energy conserving scheme, described in Eq. (20), which will be denoted as ‘‘ALTEC’’  
462 scheme.

On the sphere, considering variable Coriolis parameter ( $f = 2\Omega \sin \phi$ ) and the spherical metric terms, the original scheme (ORIG)  
is written as

$$fv \approx \frac{1}{\cos \phi} \frac{\overline{f \overline{\eta^\phi \cos(\phi) v^\lambda}}}{\eta}, \quad (21)$$

$$fu \approx \frac{\overline{f \overline{\eta^\lambda u^\phi}}}{\eta},$$

463 where  $\phi$  refers to latitude and  $\lambda$  to longitude coordinates on the sphere.

464 This scheme ensures that the Coriolis term does not contribute to the energy budget and also has steady geostrophic modes on the  
465  $f$ -sphere. Thuburn (2007) shows that it also has accurate representation of Rossby waves ( $\beta$ -effect), as the Coriolis parameter  $f$  is  
466 calculated at mass points. Unfortunately, the previous section shows that it is numerically unstable on an  $f$ -plane.

The simplified scheme (SIMP) is calculated on the sphere as

$$fv \approx \overline{f \overline{v^\phi}^\lambda}, \quad (22)$$

$$fu \approx \overline{f \overline{u^\lambda}^\phi}.$$

467 On the calculation of the energy budget, it is possible to show that no exact cancellation is expected, and therefore the Coriolis term  
468 might undesirably contributed to energy budget. Based on Thuburn (2007), it is possible to show that it also has steady geostrophic  
469 modes and accurate representation of Rossby waves. Also, it is numerically stable on an  $f$ -plane.

The alternative scheme (ALTEC) considers the Coriolis parameter calculated at vorticity points, and may be written on the sphere as

$$fv \approx \frac{1}{\cos \phi} \frac{\overline{f \overline{\eta^{\phi\lambda} \overline{\eta^\phi \cos(\phi) v^\lambda}}}}{\overline{\eta^{\phi\lambda}}}, \quad (23)$$

$$fu \approx \frac{\overline{f \overline{\eta^\lambda u^\phi}}}{\overline{\eta^{\phi\lambda}}}.$$

470 Again this matches the energy conserving scheme of Sadourny (1975). It is energy conserving and has steady geostrophic modes, but  
471 due to the position of the calculation of the Coriolis parameter at vorticity points, the  $\beta$ -effect may not be as accurate as the original  
472 scheme.

### 473 6.2.2. Numerical experiments

474 The numerical experiments will be based on the zonal flow test case with Coriolis force, as described in section 4. The experiments  
475 will be performed with the original configurations of the shallow water ENDGame scheme, with semi-Lagrangian semi-implicit  
476 discretization with  $256 \times 128$  grid points and time-step size of 1200 s.

477 A simulation run with this configuration assuming  $\eta_0 = 1\text{m}$  reveals that the original model (ORIG) is unstable. Figure 12(a) shows  
478 the error in the height field at 14.5 days, a few time-steps before the model blew up (the figure shows the step where the model attained

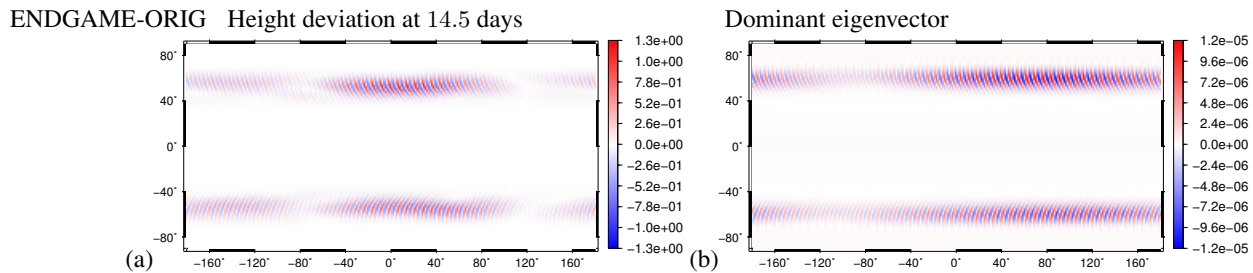


**Figure 12.** (a) Height field deviation from basic state with constant mean height of 1 m for the original ENDGame scheme at time 14.5 days. (b) Dominant eigenvector for height field deviation from basic state with constant mean height of 1 m.

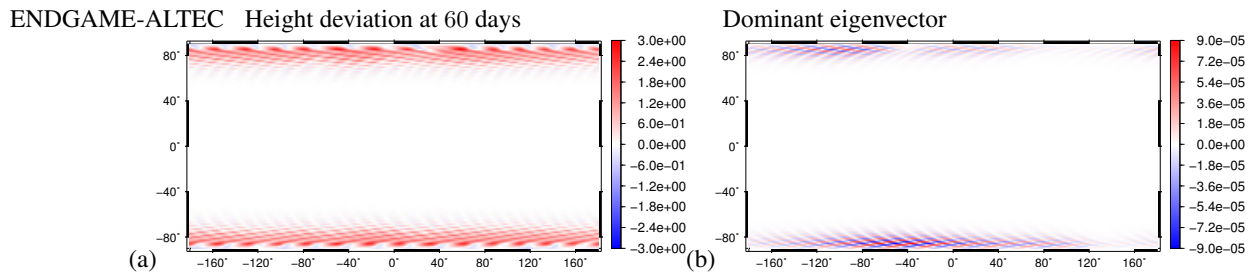


**Figure 13.** (a) Height field deviation from basic state with constant mean height of 1 m for the alternative ENDGame scheme at time 60 days. (b) Dominant eigenvector for height field deviation from basic state with constant mean height of 1 m.

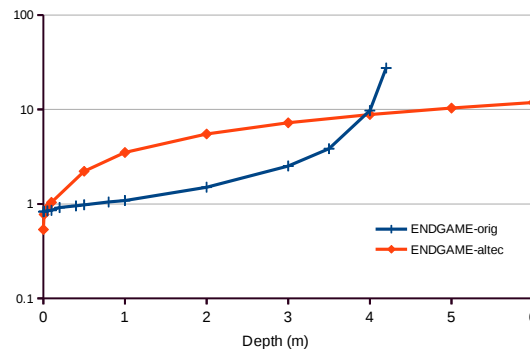


**Figure 14.** E-folding time (days) relative to different mean fluid depths (in metres) for ENDGame model.

479 maximum error in the velocity greater than  $10\text{ms}^{-1}$ ). The spherical linear analysis shows that the dominant eigenvector has larger  
 480 values concentrated over mid-latitudes (see Figure 12(b)), as happens with the error pattern observed a few time-steps before blow-up.

481 The e-folding times of the instability for different mean fluid depths ( $\eta_0$ ) are shown in Figure 14. For depths larger than 4 metres the  
 482 linear analysis method did not converge, indicating that either the model is stable, or that the methodology is not sufficiently accurate  
 483 to capture the instability. Indeed, for such larger layer depths we did not observe instability within reasonable runtime of the model (up  
 484 to 1 year).

485 The most unstable mode lies around  $60^\circ$  latitude, where, for a resolution of  $256 \times 128$  in latitude-longitude coordinates,  $f_0 \approx$   
 486  $7 \times 10^{-5}$ ,  $\Delta x \approx 78$  km and  $\Delta y \approx 156$  km, so the ratio of grid spacings is  $X \approx 0.5$ . Also, the velocity field is zonal with speed  
 487 approximately  $19\text{ms}^{-1}$  at this latitude. Therefore, we may estimate the local planar Froude number  $F_u \approx 6$  and the Rossby number  
 488  $R_u \approx 7$ . The linear analysis on the plane provides an estimate for these parameters of a maximum growth rate of approximately  
 489  $\omega f_0 \approx 6.5 \times 10^{-5}\text{s}^{-1}$ , which gives an e-folding time of about 4 hours. This is pessimistic compared to our numerical estimates of  
 490 e-folding time, which, for this scenario on the sphere, are of about 1 day (see Figure 14), but not so far off given the great deal of  
 491 approximations. Also, this scheme has implicit diffusion within the semi-Lagrangian advection, which might be responsible for the  
 492 slower growth of the instability.

493 The simple averaging scheme for the Coriolis term (SIMP) was found to be stable in all experiments performed, as predicted by the  
 494 planar linear analysis. The error of the scheme remains small throughout the experiment for long periods of time.

495 The alternative energy conserving scheme (ALTEC) was shown to be stable on the  $f$ -plane. Nevertheless, on the sphere, the variable  
 496 velocity and combination of averagings involving the depth variable and  $\cos(\phi)$  factors in the Coriolis term breaks the exact cancellation  
 497 observed on the plane. A simulation run assuming  $\eta_0 = 1$  m reveals that the alternative scheme is also unstable on the sphere, but it  
 498 takes much longer for the model to crash. Figure 13(a) shows the error in the depth field at 60 days, only a few steps before blow-up.  
 499 The unstable pattern emerging before blowing up seems to be very close to the poles. The dominant eigenvector (see Figure 13(b)) of  
 500 the most unstable mode also shows that the problem is mainly closer to the poles. A closer look at how the growth rates change with  
 501 the mean depth (see Figure 14) reveals that indeed at 1 m height the e-folding time of the alternative scheme is far larger than that of  
 502 the original scheme (about 4 times), which is approximately the extra time required for this model to blow up compared to the original  
 503 scheme. Figure 14 also shows that for larger depths (larger than 4 m), the original scheme is in fact more stable than the alternative.  
 504 A similar situation may happen if the depth is too small (smaller than 0.1 m). So, except for the interval of  $[0.01, 4]$  mean depths, the  
 505 original scheme has growth rates smaller than the alternative scheme.

## 506 6.3. Implications for 3D ENDGame

507 The three-dimensional operational ENDGame model (Wood *et al.* 2014) used at the UK MetOffice uses the original scheme (ORIG)  
 508 but in a height-based vertical coordinate with density times model layer depth as weights for the Coriolis term. In a height-based  
 509 coordinate the model layer depths are fixed and the local variations in density are relatively small. Therefore, as discussed in Section  
 510 2.2, the appropriate shallow water model to analyse the stability of 3D ENDGame is one with non-depth-weighted Coriolis terms,  
 511 similar to (22) but with some  $\cos \phi$  weights. To date no traces of this instability have been detected in the operational model, and  
 512 indeed, the above analysis suggests the model should be stable.

513 A version of 3D ENDGame with a Lagrangian vertical coordinate has been developed by Kavčić and Thurn (2017). Early versions  
 514 of that model used a depth-weighted Coriolis term, but were found to suffer from an instability with short vertical and meridional scales  
 515 that appeared in regions of strong zonal wind. Removing the depth weighting from the Coriolis term eliminated the instability. All of  
 516 these symptoms are consistent with the analysis above for the ORIG scheme.

## 517 7. Discussion and concluding remarks

518 We have proposed the use of shallow water models with very small layer depth as a useful means of investigating certain modes of  
 519 instability of three-dimensional numerical models. We have suggested a shallow water test case that is simple to implement, and also  
 520 a straightforward variant of the power method to identify the most unstable mode. In using this approach it is important to identify  
 521 which shallow water scheme corresponds to a given three-dimensional model since stability can depend crucially on the details. This  
 522 is especially true for depth weighting of vorticity or Coriolis terms, whose effects can be either stabilizing or destabilizing.

523 The results obtained for all models investigated in this paper are summarized in Table 1.

524 The finite difference energy-entropy conserving schemes (EEN and AL) were only investigated by BPT on the  $f$ -plane, and  
 525 empirical results (e.g. Lazić *et al.* 1986) seem to corroborate that the schemes are unstable for level-based models with non-depth-  
 526 weighted vorticity terms. The planar analysis indicates that these schemes are stable for depth-weighted vorticity terms, and no  
 527 evidence of instabilities in layer-based models exists to these authors' knowledge. Further investigations would be required to confirm  
 528 the stability properties of these schemes for spherical shallow water models with depth-weighted vorticity terms, which may be done  
 529 following the lines discussed in this paper.

530 A key point shown in this paper, complementing BPT, is that the Hollingsworth instability exists even without the presence of  
 531 Coriolis terms (Earth rotation). The Hollingsworth instability is due to a lack of discrete cancellation of advection terms and seems to  
 532 exist only in the presence of some background vorticity. That said, the Coriolis force can influence the Hollingsworth instability by  
 533 simply acting as a source of vorticity.

Equation	Method	Scheme	Non-depth-weighted	Depth-weighted	Observations
Vector Invariant	Finite Differences (Energy-Enst Cons)	EEN	Unstable	Stable	Stability on the $f$ -plane (Bell <i>et al.</i> 2017)
		AL	Unstable	Stable	
	Finite Volume (TRSK based)	TRSK	Unstable	Unstable	
		GASS	Unstable	Unstable	Slower growth wrt TRSK
		PXT	Unstable	Unstable	Faster growth wrt TRSK
	Finite Elements (Compound)	CUBE	-	Unstable	Faster growth wrt HEX
HEX		-	Unstable	Slower growth wrt CUBE	
Advective	Finite Differences (ENDGame)	SIMP	Stable	-	Not energy conserving
		ORIG	-	Unstable	Faster growth wrt ALTEC
		ALTEC	-	Unstable	Stable on plane

Table 1. Summary of results. Notation as defined in text. The finite element scheme was not investigated in non-depth-weighted form. For the ENDGame schemes, the simple Coriolis averaging (SIMP) does not apply to a depth-weighted form, and ORIG and ALTEC were only tested in depth-weighted form.

534 The finite volume schemes investigated, based on the TRSK scheme, all seem to be unstable, either with or without depth weighting  
 535 of vorticity terms. These analysis have direct impact, for example, on models such as MPAS (Skamarock *et al.* 2012) or DYNAMICO  
 536 (Dubos *et al.* 2015), that use this scheme. The modifications proposed by Gassmann (2013) seem to slow down the growth rate of the  
 537 instability, and is particularly beneficial for non-depth-weighted (level-based) models that run in configurations that imply very small  
 538 equivalent depths (e.g. use a Lorenz grid). For the scheme with the modifications proposed by Peixoto (2016), we see that ensuring  
 539 more accurate calculations of the terms involved in the existence of the instability is not a sufficient condition to improve the stability  
 540 properties of the scheme.

541 The finite element scheme tested in this work shows strong instabilities, particularly on the cubed-sphere grid, with slower growth  
 542 rates on the hexagonal-grid. Further analysis on the stability properties of these and other finite element schemes are currently under  
 543 investigation and will be reported elsewhere.

544 An interesting point is how the different weighting of the vorticity term influences the stability of models based on the vector invariant  
 545 momentum equations. For a depth-weighted scheme, the depth field appears in the vorticity term but does not appear in the kinetic  
 546 energy term. This suggests that the non-cancellation would be more pronounced in this case when compared to a non-depth-weighted  
 547 formulation. Indeed, our results for TRSK based schemes using very small equivalent depths ( $< 1\text{m}$ ) show that the e-folding times of  
 548 the depth-weighted formulations are smaller than the non-depth-weighted versions (see Figure 5), indicating that the instability grows  
 549 faster in depth-weighted models. Intriguingly though, BTP shows that for FD schemes on an  $f$ -plane the opposite happens: the depth-  
 550 weighted model is stable, whereas the non-depth-weighted is not. The reason is that the stability of the depth-weighted scheme shown  
 551 in BTP is not directly connected to a perfect cancellation, but related to the conservation of uniform potential vorticity (see Appendix

552 F of BPT). Further analytical inspection of the unstable modes on hexagons would be required to make a detailed connection between  
 553 the results of BTP for the een scheme and the results shown in this paper for TRSK.

554 The instability detected for the ENDGame scheme was surprising at first, since it is not in principle related to the Hollingsworth  
 555 instability, as it does not use the vector invariant momentum equations. However, it shows that the suggested test cases seem to be  
 556 applicable in a more general sense. In this case the suggested test case revealed an instability that had not been anticipated, and led us  
 557 subsequently to perform the analysis presented in section 6.1.

558 As a final point, we note that the investigation of numerical instabilities arising in shallow water systems considering small equivalent  
 559 depths seems to be not only of theoretical interest, but of practical importance. Non-idealised weather and ocean models indeed possess  
 560 vertical modes corresponding to very small equivalent depths and may be subject to these instabilities. The main purpose of this paper  
 561 was not to show solutions to stability issues, but more to enlighten the investigation path with tools and better understanding of such  
 562 instabilities.

## 563 Acknowledgements

564 Peixoto acknowledges the Sao Paulo Research Foundation (FAPESP) under the grant number 2016/18445-7 and the National Science  
 565 and Technology Development Council (CNPq) under grant number 441328/2014-8. Thuburn was funded by the Natural Environment  
 566 Research Council under the ‘‘Gung Ho’’ project (grant NE/1021136/1). Bell was supported by the Joint UK DECC/Defra Met Office  
 567 Hadley Centre Climate Programme (GA01101).

## 568 A. Linear analysis for the ‘een’ scheme with no Coriolis force

569 In this section we follow the analysis of BPT to show that with a constant velocity basic state and null Coriolis force ( $f_0 = 0$ ) the  
 570 original ‘een’ scheme is neutrally stable on a plane.

Using the same notation as in BPT, one may write the linearized form of the shallow water equations for the height coordinate model,  
 ignoring the Coriolis term, as (see equations (61-62) of BPT)

$$\begin{aligned} \frac{\partial u'}{\partial t} + g\delta_x \eta' + u_1 \delta_x \bar{u}^x + v_1 \delta_y \bar{u}^{y\mu E} + \\ v_1 \delta_x (\bar{v}^y - \bar{v}^{y\mu E}) &= 0, \\ \frac{\partial v'}{\partial t} + g\delta_y \eta' + u_1 \delta_x \bar{v}^{x\nu E} + v_1 \delta_y \bar{v}^y + \\ u_1 \delta_y (\bar{u}^x - \bar{u}^{x\nu E}) &= 0, \\ \frac{\partial \eta'}{\partial t} + u_1 \delta_x \bar{\eta}^x + v_1 \delta_y \bar{\eta}^y + \\ \eta_0 (\delta_x u' + \delta_y v') &= 0, \end{aligned} \quad (24)$$

571 where the basic state has constant velocities ( $u_1, v_1$ ) and constant depth  $\eta_0$  and the system refers to the perturbed variables for velocity  
 572 and depth (primed variables).

573 Let us assume wave-like solutions as

$$(u', v', \eta') = (\hat{u}, \hat{v}, \hat{\eta}) \exp\left(\frac{i\kappa x}{\Delta x} + \frac{i\lambda y}{\Delta y} - i\omega t\right), \quad (25)$$

574 where  $\omega$  is the frequency and  $(\kappa, \lambda)$  are non-dimensional horizontal wavenumbers for the  $x$ - and  $y$ -directions normalised using the grid  
 575 spacings  $\Delta x$  and  $\Delta y$  respectively. Substituting the wave-like forms in the perturbation equations, and using that, for a quantity  $\psi$ , the  
 576  $x$ - and  $y$ -averaging operators and the differencing operators  $\delta_x$  and  $\delta_y$  give, respectively,

$$\bar{\psi}^x = c_\kappa \psi, \quad \bar{\psi}^y = c_\lambda \psi, \quad (26)$$

577

$$\delta_x \psi = \frac{2i}{\Delta x} s_\kappa \psi, \quad \delta_y \psi = \frac{2i}{\Delta y} s_\lambda \psi, \quad (27)$$

one obtains the following linear system,

$$\begin{bmatrix} \omega - E_{11} & E_{12} & -\frac{2}{\Delta x} c s_\kappa \\ E_{21} & \omega - E_{22} & -\frac{2}{\Delta y} c s_\lambda \\ -\frac{2}{\Delta x} c s_\kappa & -\frac{2}{\Delta y} c s_\lambda & \omega - E_{33} \end{bmatrix} \begin{bmatrix} \hat{u} \\ \hat{v} \\ \frac{c\hat{\eta}}{H} \end{bmatrix} = 0, \quad (28)$$

where,

$$\begin{aligned} E_{11} &= \frac{2u_1}{\Delta x} s_\kappa c_\kappa + \frac{2v_1}{\Delta y} s_\lambda c_\lambda \mu E, \\ E_{22} &= \frac{2u_1}{\Delta x} s_\kappa c_\kappa \nu E + \frac{2v_1}{\Delta y} s_\lambda c_\lambda, \\ E_{33} &= \frac{2u_1}{\Delta x} s_\kappa c_\kappa + \frac{2v_1}{\Delta y} s_\lambda c_\lambda, \\ E_{12} &= \frac{2v_1}{\Delta x} s_\kappa c_\lambda (\mu E - 1), \\ E_{21} &= \frac{2u_1}{\Delta y} s_\lambda c_\kappa (\nu E - 1). \end{aligned} \quad (29)$$



578 As in BPT,

$$\mu_E = \frac{1}{3}(1 + 2c_\kappa^2), \quad \nu_E = \frac{1}{3}(1 + 2c_\lambda^2), \quad (30)$$

579 and  $c$ ,  $c_\kappa$ ,  $c_\lambda$ ,  $s_\kappa$  and  $s_\lambda$  are defined in Eqs. (14) and (16).

580 It will be convenient to introduce

$$T_u \equiv \frac{2u_1}{\Delta x} c_\kappa (1 - \nu_E), \quad T_v \equiv \frac{2v_1}{\Delta y} c_\lambda (1 - \mu_E). \quad (31)$$

581 Using these definitions with (29) one sees that

$$E_{11} = E_{33} - T_v s_\lambda, \quad E_{22} = E_{33} - T_u s_\kappa, \quad (32)$$

582 and the matrix (28) becomes

$$\begin{bmatrix} \varpi + T_v s_\lambda & T_v \frac{s_\kappa}{X} & -\frac{2}{\Delta x} c s_\kappa \\ T_u X s_\lambda & \varpi + T_u s_\kappa & -\frac{2}{\Delta y} c s_\lambda \\ -\frac{2}{\Delta x} c s_\kappa & -\frac{2}{\Delta y} c s_\lambda & \varpi \end{bmatrix} \begin{bmatrix} \hat{u} \\ \hat{v} \\ \frac{c\hat{\eta}}{H} \end{bmatrix} = 0, \quad (33)$$

583 in which

$$\varpi = \omega - E_{33} = \omega - \frac{2u_1}{\Delta x} s_\kappa c_\kappa - \frac{2v_1}{\Delta y} s_\lambda c_\lambda \quad (34)$$

584 is the Doppler-shifted non-dimensional frequency of the perturbation and  $X = \Delta x / \Delta y$ .

585 By direct calculation of the determinant  $D_M$  of the matrix in (33), one finds that

$$D_M = \varpi^3 + P\varpi^2 - Q^2\varpi - PQ^2, \quad (35)$$

586 where

$$P = T_u s_\kappa + T_v s_\lambda, \quad (36)$$

$$Q^2 = \left( \frac{2s_\kappa c}{\Delta x} \right)^2 + \left( \frac{2s_\lambda c}{\Delta y} \right)^2.$$

587 Substituting  $\varpi = -P$  into (35) one sees that it is a solution of  $D_M = 0$ . Hence it is easy to factorise (35),

$$D_M = (\varpi + P)(\varpi^2 - Q^2). \quad (37)$$

588 The solutions of  $D_M = 0$ ,  $\varpi = \pm Q$  and  $\varpi = -P$ , are real valued, so the system is neutrally stable.

## 589 B. Linear analysis on the sphere

590 In this appendix we describe an algorithm to evaluate the eigen-structure of the most unstable modes using a nonlinear shallow water code modified to apply a variation of the power method to small perturbations.

592 Let  $x^{(k)}$  be the vector of values representing the model state at time step  $k$  and let  $G$  represent the action of the nonlinear shallow water model integration scheme over one time step, so that the unmodified shallow water model obeys

$$x^{(k+1)} = G(x^{(k)}). \quad (38)$$

594 We are interested in the evolution of perturbations to some basic state  $\bar{x}$ , which should be steady. In practice, for a given numerical method it may be difficult or impossible to find a state close to the desired basic state that satisfies  $\bar{x} = G(\bar{x})$ . Therefore a constant forcing term  $F = \bar{x} - G(\bar{x})$  is introduced to compensate for the numerical drift of the desired basic state;  $F$  is easily computed by taking one model time step from the state  $\bar{x}$ . The model governing equation (Eq. (38)) is then replaced by

$$x^{(k+1)} = G(x^{(k)}) + F. \quad (39)$$

598 Clearly  $\bar{x}$  is now a steady solution for the model (39). Note that  $F$  must be a constant forcing, not a relaxation back towards the basic state; such a relaxation would damp perturbations and so affect the diagnosed eigenmode growth rates.

600 Now consider the evolution of a small perturbation  $y^{(k)}$  to the basic state, so that  $x^{(k)} = \bar{x} + y^{(k)}$ . Linearizing (39) gives

$$y^{(k+1)} = G'(\bar{x})y^{(k)} + O(2), \quad (40)$$

601 where  $G'(\bar{x})$  is the Jacobian matrix of the model evolution operator evaluated for the state  $\bar{x}$ , and  $O(2)$  denotes higher (second) order terms in  $y^{(k)}$ . It is the dominant eigenvalue and eigenvector of  $G'$  that we wish to determine. Provided  $y$  remains small, taking repeated model time steps according to (39) will cause  $y$  to evolve according to (40) with  $O(2)$  negligible, and  $y$  should evolve towards the dominant eigenvector of  $G'$ , as in the power method.

605 However, with this method, it is likely that  $y$  fails to remain small and so the linearization breaks down before the dominant eigenvector emerges. Therefore, another modification is needed to the model to rescale perturbations to ensure they remain small. Thus we take a preliminary step forward using the model with constant forcing

$$x^* = G(x^{(k)}) + F, \quad (41)$$

608 diagnose the perturbation

$$r^{(k+1)} = x^* - \bar{x}, \quad (42)$$

609 then rescale the perturbation before computing the state at the new time level

$$x^{(k+1)} = \alpha_{k+1} r^{(k+1)} + \bar{x}. \quad (43)$$

610 Here  $\alpha_{k+1} = \epsilon / \|r^{(k+1)}\|$ , for  $\epsilon > 0$  a small constant. Iterating (41)-(43) should then determine the same eigenvector as the power  
611 method applied to  $G'$ .

612 If the method converges then the absolute value of the dominant eigenvalue ( $\lambda$ ) may be obtained using the converged value of  $\alpha_k$ ,  
613 which we will denote simply as  $\alpha$ , as  $\lambda = 1/\alpha$ .

614 Provided the basic state is fluid-dynamically stable, the shallow water equations should not have any growing modes. Then, for a  
615 stable numerical scheme, it is expected that  $\lambda = 1$  for any parameter choice. The unstable modes are detected when  $\lambda > 1$  ( $\alpha < 1$ ),  
616 and, in this case, the associated eigenvector will be given by the converged vector  $y$ .

617 The growth rate ( $\nu$ ) may be then obtained observing that  $\lambda = e^{\nu \Delta t}$ , where  $\Delta t$  is the time-step used in the calculation of  $G$ .  
618 Consequently, the e-folding time (time for the instability to grow by a factor of  $e$ ), may be also calculated directly from  $\nu$ .

619 In our experiments we adopted  $\epsilon = 1 \times 10^{-5}$  and the 2 norm of the velocity field for calculation of  $\alpha_k$ . A small local perturbation  
620 was added to the initial height field to trigger any unstable modes. This approach can usually be easily incorporated in standard shallow  
621 water model codes.

622 Some important points must be made with respect to the application of this scheme and the interpretation of its results. First, we  
623 are assuming that the forcing  $F$  is small. For the basic states used in this paper, which are all in analytical balance,  $F$  represents  
624 the numerical error between the numerical adjustment with respect to the analytical steady state; therefore should be limited to local  
625 truncation errors, and thus small. Second, the eigenvalues might not necessarily be well separated, which means that the eigenvector  
626 obtained might not always match the dominant pattern appearing in a full model run. This lack of matching might also happen due to  
627 nonlinear effects influencing the full model run. Therefore, if the method converges, we have as result one of the possible dominant  
628 eigenmodes, which is enough to show that the model is linearly unstable and will provide estimates of the instability growth rate.

## 629 References

- 630 Arakawa A. 2000. A personal perspective on the early years of general circulation modeling at UCLA. In: *General circulation model development*, Randall DA  
631 (ed), International Geophysics Series, 70, Academic Press, pp. 1–65.
- 632 Arakawa A, Lamb VR. 1981. A potential enstrophy and energy conserving scheme for the shallow water equations. *Mon. Weather Rev.* **109**: 18–36.
- 633 Barros SRM, Garcia CI. 2004. A global semi-implicit semi-lagrangian shallow-water model on locally refined grids. *Monthly Weather Review* **132**(1): 53–65.
- 634 Bell MJ, Peixoto PS, Thuburn J. 2017. Numerical instabilities of vector-invariant momentum equations on rectangular C-grids. *Quarterly Journal of the Royal  
635 Meteorological Society* **143**(702): 563–581.
- 636 Bleck R, Boudra DB. 1981. Initial testing of a numerical ocean circulation model using a hybrid (quasi-isopycnic) vertical coordinate. *Journal of Physical  
637 Oceanography* **11**(6): 755–770.
- 638 Burridge DM, Haseler JC. 1977. A model for medium range weather forecasting. *ECMWF Tech. Report* **4**.
- 639 Daley R. 1988. The normal modes of the spherical non-hydrostatic equations with applications to the filtering of acoustic modes. *Tellus A: Dynamic Meteorology  
640 and Oceanography* **40**(2): 96–106.
- 641 Dubos T, Dubey S, Tort M, Mittal R, Meurdesoif Y, Hourdin F. 2015. DYNAMICO-1.0, an icosahedral hydrostatic dynamical core designed for consistency and  
642 versatility. *Geoscientific Model Development* **8**(10): 3131–3150.
- 643 Ducoussou N, Sommer JL, Molines JM, Bell M. 2017. Impact of the Symmetric Instability of the Computational Kind at mesoscale and submesoscale permitting  
644 resolutions. *Ocean Modelling* : in review.
- 645 Galewsky J, Scott RK, Polvani LM. 2004. An initial-value problem for testing numerical models of the global shallow-water equations. *Tellus A* **56**(5): 429–440.
- 646 Gassmann A. 2011. Inspection of hexagonal and triangular c-grid discretizations of the shallow water equations. *J. Comput. Phys.* **230**(7): 2706–2721.
- 647 Gassmann A. 2013. A global hexagonal C-grid non-hydrostatic dynamical core (ICON-IAP) designed for energetic consistency. *Quart. J. Roy. Meteorol. Soc.*  
648 **139**: 152–175.
- 649 Gill AE. 1982. *Atmosphere-ocean dynamics*. Academic Press.
- 650 Heikes R, Randall DA. 1995. Numerical integration of the shallow-water equations on a twisted icosahedral grid. Part I: basic design and results of tests. *Mon.  
651 Wea. Rev.* **123**(6): 1862–1880.
- 652 Hollingsworth A, Kallberg P, Renner V, Burridge DM. 1983. An internal symmetric computational instability. *Quart. J. Roy. Meteor. Soc.* **109**: 417–428.
- 653 Holton JR, Hakim GJ. 2012. *An introduction to dynamic meteorology*, vol. 88. Academic press.
- 654 Hsu YJG, Arakawa A. 1990. Numerical modeling of the atmosphere with an isentropic vertical coordinate. *Monthly Weather Review* **118**(10): 1933–1959.
- 655 Jablonowski C, Williamson DL. 2006. A baroclinic instability test case for atmospheric model dynamical cores. *Quarterly Journal of the Royal Meteorological  
656 Society* **132**(621C): 2943–2975.
- 657 Ju L, Ringler TD, Gunzburger M. 2011. Voronoi tessellations and their application to climate and global modeling. In: *Numerical Techniques for Global  
658 Atmospheric Models, Lecture Notes in Computational Science and Engineering*, vol. 80, Lauritzen P, Jablonowski C, Taylor M, Nair R (eds), Springer Berlin  
659 Heidelberg, pp. 313–342.
- 660 Kasahara A, Puri K. 1981. Spectral representation of three-dimensional global data by expansion in normal mode functions. *Monthly Weather Review* **109**(1):  
661 37–51.
- 662 Kavčić I, Thuburn J. 2017. A Lagrangian vertical coordinate version of the ENDGame dynamical core, Part I: Formulation, remapping strategies, and robustness.  
663 *Manuscript in preparation* .
- 664 Lauritzen PH, Jablonowski C, Taylor MA, Nair RD. 2011. *Numerical techniques for global atmospheric models*, vol. 80. Springer Science & Business Media.
- 665 Lazić J, Janjić Z, Mesinger F. 1986. Non-cancellation instability in horizontal advection schemes for momentum equations. *Meteor. Atmos. Phys.* **35**, **1**: 49–52.
- 666 Lin SJ. 2004. A “vertically lagrangian” finite-volume dynamical core for global models. *Monthly Weather Review* **132**(10): 2293–2307.
- 667 McDonald A, Bates J. 1989. Semi-lagrangian integration of a gridpoint shallow water model on the sphere. *Monthly Weather Review* **117**(1): 130–137.
- 668 Peixoto PS. 2016. Accuracy analysis of mimetic finite volume operators on geodesic grids and a consistent alternative. *Journal of Computational Physics* **310**:  
669 127 – 160.
- 670 Peixoto PS, Barros SRM. 2013. Analysis of grid imprinting on geodesic spherical icosahedral grids. *J. Comput. Phys.* **237**: 61 – 78.
- 671 Ringler T, Petersen M, Higdon RL, Jacobsen D, Jones PW, Maltrud M. 2013. A multi-resolution approach to global ocean modeling. *Ocean Modelling* **69**(0):  
672 211 – 232.

- 673 Ringler TD, Thuburn J, Klemp JB, Skamarock WC. 2010. A unified approach to energy conservation and potential vorticity dynamics for arbitrarily-structured  
674 C-grids. *J. Comput. Phys.* **229**(9): 3065 – 3090.
- 675 Sadourny R. 1975. The dynamics of finite-difference models of the shallow water equations. *J. Atmos. Sci.* **32**: 680–689.
- 676 Shamir O, Paldor N. 2016. A quantitative test case for global-scale dynamical cores based on analytic wave solutions of the shallow-water equations. *Quarterly*  
677 *Journal of the Royal Meteorological Society* **142**(700): 2705–2714.
- 678 Skamarock WC, Klemp JB, Duda MG, Fowler LD, Park SH, Ringler TD. 2012. A Multiscale Nonhydrostatic Atmospheric Model Using Centroidal Voronoi  
679 Tessellations and C-Grid Staggering. *Mon. Wea. Rev.* **140**: 3090–3105.
- 680 Skamarock WC, Klemp JB, Duda MG, Fowler LD, Park SH, Ringler TD. 2012. A multiscale nonhydrostatic atmospheric model using centroidal Voronoi  
681 tessellations and C-grid staggering. *Mon. Weath. Rev.* **140**: 3090–3105.
- 682 Staniforth A, Thuburn J. 2012. Horizontal grids for global weather and climate prediction models: a review. *Quart. J. R. Met. Soc.* **138**(662): 1–26.
- 683 Terasaki K, Tanaka H. 2007. An analysis of the 3-d atmospheric energy spectra and interactions using analytical vertical structure functions and two reanalyses.  
684 *Journal of the Meteorological Society of Japan. Ser. II* **85**(6): 785–796.
- 685 Thuburn J. 2007. Rossby wave dispersion on the c-grid. *Atmospheric Science Letters* **8**(2): 37–42.
- 686 Thuburn J, Cotter CJ. 2015. A primal-dual mimetic finite element scheme for the rotating shallow water equations on polygonal spherical meshes. *J. Comput.*  
687 *Phys.* **290**(C): 274–297.
- 688 Thuburn J, Cotter CJ, Dubos T. 2014. A mimetic, semi-implicit, forward-in-time, finite volume shallow water model: comparison of hexagonal-icosahedral and  
689 cubed-sphere grids. *Geoscientific Model Development* **7**(3): 909–929.
- 690 Thuburn J, Ringler TD, Skamarock WC, Klemp JB. 2009. Numerical representation of geostrophic modes on arbitrarily structured C-grids. *J. Comput. Phys.*  
691 **228**: 8321–8335.
- 692 Thuburn J, Staniforth A. 2004. Conservation and Linear Rossby-Mode Dispersion on the Spherical C Grid. *Monthly Weather Review* **132**(2): 641–653.
- 693 Tomita H, Goto K, Satoh M. 2008. A New Approach to Atmospheric General Circulation Model: Global Cloud Resolving Model NICAM and its Computational  
694 Performance. *SIAM J. Sci. Comput.* **30**(6): 2755–2776.
- 695 Tribbia J, Temam R. 2011. Waves, hyperbolicity and characteristics. In: *Numerical Techniques for Global Atmospheric Models*, Springer, pp. 29–42.
- 696 Vallis GK. 2006. *Atmospheric and oceanic fluid dynamics*. Cambridge University Press.
- 697 Wan H, Giorgetta MA, Zängl G, Restelli M, Majewski D, Bonaventura L, Fröhlich K, Reinert D, Rípodas P, Kornblueh L, Förstner J. 2013. The ICON-1.2  
698 hydrostatic atmospheric dynamical core on triangular grids. Part 1: Formulation and performance of the baseline version. *Geoscientific Model Development*  
699 **6**(3): 735–763.
- 700 Weller H, Thuburn J, Cotter CJ. 2012. Computational modes and grid imprinting on five quasi-uniform spherical C-grids. *Mon. Wea. Rev.* **140**(8): 2734–2755.
- 701 Williamson DL, Drake JB, Hack JJ, Jakob R, Swarztrauber PN. 1992. A standard test set for numerical approximations to the shallow water equations in  
702 spherical geometry. *J. Comput. Phys.* **102**(1): 211–224.
- 703 Wood N, Staniforth A, White A, Allen T, Diamantakis M, Gross M, Melvin T, Smith C, Vosper S, Zerroukat M, Thuburn J. 2014. An inherently mass-conserving  
704 semi-implicit semi-Lagrangian discretization of the deep-atmosphere global non-hydrostatic equations. *Quarterly Journal of the Royal Meteorological Society*  
705 **140**(682): 1505–1520.
- 706 Zerroukat M, Wood N, Staniforth A, White AA, Thuburn J. 2009. An inherently mass-conserving semi-implicit semi-lagrangian discretisation of the shallow-  
707 water equations on the sphere. *Quarterly Journal of the Royal Meteorological Society* **135**(642): 1104–1116.